Fluid-Rock Characterization for NMR Well Logging and Special Core Analysis

3nd Annual and Final Report

January 1, 2007 – December 31, 2007

George J. Hirasaki (gjh@rice.edu)

and

Kishore K. Mohanty (mohanty@uh.edu)

Issued: March 2008

DE-FC26-04NT15515

Project Officer:
Chandra Nautiyal, Tulsa

Contract Officer:
Thomas J. Gruber, Pittsburg

Rice University
6100 Main Street
Houston, TX 77005

University of Houston
4800 Calhoun Road
Houston, TX 77204-4004

DISCLAIMER* — The Disclaimer must follow the title page, and must contain the following paragraph:

"This report was prepared as an account of work sponsored by an agency of the United States Government. Neither the United States Government nor any agency thereof, nor any of their employees, makes any warranty, express or implied, or assumes any legal liability or responsibility for the accuracy, completeness, or usefulness of any information, apparatus, product, or process disclosed, or represents that its use would not infringe privately owned rights. Reference herein to any specific commercial product, process, or service by trade name, trademark, manufacturer, or otherwise does not necessarily constitute or imply its endorsement, recommendation, or favoring by the United States Government or any agency thereof. The views and opinions of authors expressed herein do not necessarily state or reflect those of the United States Government or any agency thereof."

ABSTRACT

Need for Project

NMR well logging provides a record of formation porosity, permeability, irreducible water saturation, oil saturation and viscosity. In the absence of formation material, the NMR logs are interpreted using default assumptions. Special core analysis on core samples of formation material provides a calibration between the log response and the desired rock and/or fluid property. The project proposes to develop interpretations for reservoirs that do not satisfy the usual assumptions inherent in the interpretation. Also, NMR will be used in special core analysis to investigate the mechanism of oil recovery by wettability alteration and the relative permeability of non-water-wet systems.

Some common assumptions and the reality of exceptional reservoirs are listed in the following and will be addressed in this project.

(1) *Assumption*: in situ live crude oil and OBM have a relaxation time proportional to temperature/viscosity as correlated from stock tank oils. *Reality*: methane and ethane relax by a different mechanism than for dead oil and GOR is a parameter; carbon dioxide does not respond to proton NMR but influences oil and gas viscosity and relaxation rates.

(2) *Assumption*: the in situ hydrocarbons have a relaxation time equal to that of the bulk fluid, i.e. there is no surface relaxation as if the formation is water-wet. *Reality*: Most oil reservoirs are naturally mixed-wet and drilling with oil-based mud (OBM) sometimes alters wettability. If the formation is not water-wet, surface relaxation of the hydrocarbon will result.

(3) *Assumption*: OBM filtrate has the properties of the base oil. *Reality*: OBM filtrate often has some level of the oil-wetting additives and in some cases has paramagnetic particles. It may also have dissolved gas.

(4) *Assumption*: the magnetic field gradient is equal to that of the logging tool. *Reality*: paramagnetic minerals may result in internal magnetic field gradient much greater than that of the logging tool.

(5) *Assumption*: pores of different size relax independently. *Reality*: clay lined pores can have significant diffusional coupling between microporosity and macroporosity.

Abstract for Year 3

Year 3 reports on two subtasks: Subtask 1.1 Properties of live reservoir fluids with report on, “NMR Measurement of Bitumen at Different Temperatures” and Subtask 2.3 Transverse relaxation in sandstones due to the presence of Internal Field Gradients.

Abstract from Year 1

Progress is reported on Tasks: (1.2) Properties of oil-based drilling fluids, (2.2) Application of restricted diffusion for characterization of vuggy carbonate formations, (2.4) Interpretation of systems with diffusional coupling between pores, and (3) Characterization of pore structure and wettability.

Abstract from Year 2

Progress is reported on Tasks: (1.1) Properties of live reservoir fluids, (2.1) Extend the diffusion editing technique and interpretation, (2.4) Interpretation of systems with diffusional coupling between pores, (2.5) Quantify the mechanisms responsible for the deviation of surface relaxivity from the mean value for sandstones and carbonates, and (3) Characterization of pore structure and wettability.

TABLE OF CONTENTS

EXECUTIVE SUMMARY

Year 3

NMR Measurement of Bitumen at Different Temperatures

NMR well logging for bitumen is challenging because the bitumen usually has components of the T_2 distribution that are shorter than the echo spacing and thus are not captured. We show that more accurate measurements of the T_2 distribution can be made if the CPMG data is supplemented with FID (free induction decay) data. Also, an assumption is made that the shape of the T_2 distribution of the bitumen is a log-normal distribution. This approach gives reliable results at sample temperatures of about 60 °C but it suffers from lack of early data in the FID at low temperatures.

Transverse relaxation in sandstones due to the presence of Internal Field Gradients

Measurements of T_2 are seriously compromised in sandstone with paramagnetic chlorite coating sand grains. The NMR response of due to the internal gradients in model clay-lined pores is modeled for a systematic investigation and characterization of such systems.

Years 1 and 2

Task 1 is on the NMR properties of reservoir fluids. Mixtures of crude oil contaminated with oil based drilling fluids were described. A research program to verify a mixing model for natural gas mixtures was initiated.

Task 2 is the estimation of rock properties from relaxation and diffusion. Significant advances were made on the understanding of diffusion coupling between micro- and macro-porosity and the mechanisms for diffusion relaxation with internal gradients. Estimation of diffusion coupling between vugs and matrix was limited by relaxation before significant coupling could be measured. However, methodology to measure pore size distribution by simultaneous relaxation and restricted diffusion was refined. A method to quantify wettability with a NMR wettability index was developed.

Task 3 was on characterization of pore structure and wettability. Characterization of pore structure and wettability was completed on six carbonate samples. The vug size, distribution and interconnection vary significantly in these six samples.

Subtask 1.1 Properties of live reservoir fluids

NMR Measurement of Bitumen at Different Temperatures

(Yang and Hirasaki, 2008)

Abstract

Heavy oil (bitumen) is characterized by its high viscosity and density, which is a major obstacle to both well logging and recovery. Due to the lost information of T_2 relaxation time shorter than echo spacing (TE) and interference of water signal, estimation of heavy oil properties from NMR T_2 measurements is usually problematic. In this work, a new method has been developed to overcome the echo spacing restriction of NMR spectrometer during the application to heavy oil (bitumen). A FID measurement supplemented the start of CPMG. Constrained by its initial magnetization (M_0) estimated from the FID and assuming log normal distribution for bitumen, the corrected T_2 relaxation time of bitumen sample can be obtained from the interpretation of CPMG data. This new method successfully overcomes the TE restriction of the NMR spectrometer and is nearly independent on the TE applied in the measurement.

This method was also applied to the measurement at elevated temperatures (8 ~ 90 ^{o}C). In order to rectify the incorrect dependence of extrapolated M_0 on temperature resulting from the loss of FID signal within initial decay period, the apparent M_0 at high temperature (60 ^{o}C) was reasonably assumed to be the real value, on the basis of which, Curie's Law was employed to estimate the M_0 of bitumen sample at other temperatures. Consequently, some important petrophysical properties, such as hydrogen index (*HI*), fluid content and viscosity of bitumen were evaluated by using corrected T_2.

Keywords: Well logging; bitumen; Relaxation time; Lognormal distribution; Curie's Law

1 Introduction

Heavy oil and bitumen is characterized by its high viscosity and density, and represent a worldwide known oil reserve of 6 trillion barrels [1] and [2]. As the conventional oil reserves of the world continue to decline and the exploration and production technologies keep improving, the heavy oil and bitumen deposits have attracted great attention from both the government and the industry, and will be the future of the world oil industry for years to come.

Low field NMR has displayed great potential in many heavy oil well logging cases (California, Venezuela, China) [2]. However, the high oil viscosity still put challenging problems to the NMR logging tools. The echo spacing (TE) limitation of applied NMR logging instrument and the fast relaxation of heavy oil resulting from its high viscosity have combined to make the NMR information (T_2) inevitably get lost during measurements [3], [4], [5], [6], [7], [8], [9], [10] and [11]. Consequently, estimation of bitumen properties, such as hydrogen index (*HI*), fluid content and viscosity, based on the captured NMR response is problematic and generally has incorrect TE or sample temperature dependence.

Kleinberg and Vinegar [3] reported an apparent hydrogen index (HI_{app}) decrease among NMR measurements on some heavy crude oil samples (API gravity < 17^o) and attributed it to the oil components decaying faster than 1 msec. LaTorraca, *et al*. [6] investigated on the effects of varying TE on the T_2 distributions and incorporate TE as a parameter into the Vinegar equation [3] to relate the signal loss (HI_{app} or apparent logarithmic mean T_2, $T_{2,app}$) to the viscosity for heavy oils (>1000 cp).

However, this particular method, which based on the signal loss in NMR measurement on heavy oils, has inevitable dependence on the value of TE used by the NMR logging tools and need consequent adjustment according to different TE applied. Furthermore, using these signal-loss-based correlations have to combine other logging tools, such as the use of resistivity and density logs for porosity and oil saturation, and estimates of the degree of invasion. The influences from high noise levels on any of these logging tools will bring error into the estimates. More importantly, the essential use of those “apparent” NMR values (HI_{app} or $T_{2,app}$) in this method makes it lose the possibility to develop the ultimate theory-based correlations for oil properties, which undoubtedly depend on the “real” values.

In this work, the new methods for both NMR measurement and subsequent raw data interpretation are developed to correct the T_2 relaxation times of heavy oil (bitumen). The new methods can overcome the echo spacing limitation of NMR spectrometer and have only minor TE dependence. Further improvement was also made to eliminate the incorrect temperature dependence during the application of the new methods at different sample temperatures (8 ~ 90 ^{o}C). The petrophysical properties, such as hydrogen index, fluid saturation and viscosity are able to be directly estimated from the corrected relaxation times.

2 Equipment and Experimental Procedures

The major nuclear magnetic resonance (NMR) spectrometer used in this work is a low field Maran-II spectrometer, which is operating at a proton resonance frequency of 2.0 MHz. The effective vertical height of the magnetic field is around 5 cm. The temperature of magnetic field system is controlled at 30 ^{o}C with an error of ± 0.1 ^{o}C.

The heavy oil sample used in this work is froth separated Athabasca bitumen from Alberta, Canada. It consists of bitumen, water and a small amount of clay. The bitumen sample used for the measurements with Maran-II is contained in a glass tube (I.D. 4.66 cm) with a sample height of 3.60 cm. The sample tube was carefully sealed and stored at room temperature.

The NMR measurements were performed at different sample temperatures from 8 to 90 ^{o}C. The temperature of magnet was kept at 30 ^{o}C for all measurements. Before each measurement, the bitumen sample was placed in a thermal water bath with interested temperature for over 4 hours to reach the sample temperature equilibrium. The sample tube was wrapped with four-layer paper insulation during the measurement. A single measurement took less than 1 min. The measurement at each temperature was repeated at least three times to ensure the data reliabilities.

The 90 ^{o}C case was employed to demonstrate the temperature change during heating process and NMR measurement. The temperature at the center was used to represent the bitumen sample temperature. As shown in Fig. 1, it only took about 90 min. to heat the bitumen sample from room temperature to 90 ^{o}C. The sample was equilibrated for over 4 hours. During the subsequent NMR measurement, the sample temperature deviation was 1.6 % within 1 min. 90 ^{o}C is the highest temperature used in this work and has the largest temperature difference from the magnet temperature (30 ^{o}C). According to the results displayed in Fig. 1, it is reasonable to assume that 4-hour thermal water bath was enough to reach equilibrium at any interested temperature in this work. And the temperature deviation during the measurement was acceptable.

3 Results

3.1 Regular CPMG Measurement on Bitumen Sample

Regular CPMG measurements were performed on the Athabasca bitumen sample of 30 ^{o}C with the Maran-II spectrometer. Three different echo spacings (TE) 0.4 msec, 0.8 msec and 1.2 msec were applied respectively. The CPMG raw data were fitted to the standard multi-exponential decay model as follow [12]:

$$M(t) = \sum_i f_i \cdot e^{-\frac{t}{T_{2,i}}} \quad (1)$$

The interpreted T_2 relaxation time distributions of this bitumen sample were shown in Fig. 2. It is clear that, the T_2 distribution of bitumen sample has a strong

dependence on the applied echo spacing. When the echo spacing increases, the bitumen peak shifts to the larger relaxation time, while the area of the bitumen peak significantly decreases. It implies that, due to the short T_2 relaxation time (less than 1 msec) of bitumen resulting from its high viscosity (on the order of 10^6 cp), the T_2 of some components of bitumen is even shorter than the echo spacing of the NMR spectrometer. Therefore, as larger echo spacing was applied, more T_2 distribution information of bitumen was lost.

Another observation that can be made from Fig. 2 is that the bitumen signal and water signal are separated clearly in the T_2 relaxation time distribution at 30 ^{o}C. The entire signal from the bitumen is found in the first peak of the sample spectra. Thus, in this case, the local minimum after the bitumen peak was employed as the cut-off between oil and water peaks.

The NMR responses (amplitude *f*) from water and bitumen in the sample are calculated respectively and shown in Table 1. We can easily find that, due to the loss of T_2 information shorter than the applied echo spacing, the summation of amplitude from bitumen keeps deceasing when the applied echo spacing increases. On the other hand, the summation of amplitudes from the water response, which can be taken as the indication of area covered by water peaks, only has very slight changes. This implies insensitive response of water to the applied echo spacing, which results from its significantly lower viscosity and larger T_2 relaxation time.

3.2 Improved Experimental Scheme for Correcting T_2 of Bitumen

In order to overcome the inevitable echo spacing restriction of Maran-II, a modified scheme for CPMG measurement was developed to correct the T_2 relaxation time of bitumen. In this new scheme, a regular FID was imposed at the start of each CPMG measurement. Then the initial magnetization of the bitumen sample M_0, can be obtained from the extrapolation of FID as shown in Fig. 3.

The transverse relaxation of the measured FID signal follows a first order rate process with a characteristic time constant T_2^* [13]:

$$M(t) = M_0 \cdot e^{-\frac{t}{T_2^*}}. \qquad (2)$$

Here, M_0 is the initial magnetization of the sample. The constant T_2^* is called transverse relaxation time and affected by the inhomogeneity of the static magnetic field. The time constant describing the decay of the transverse magnetization due to both the spin-spin relaxation of bulk sample (T_2) and the inhomogeneity of the static field is given as:

$$\frac{1}{T_2^*} = \frac{1}{T_{2,b}} + \gamma \cdot \Delta B_0 . \qquad (3)$$

where $T_{2,b}$ is the intrinsic transverse relaxation time of bitumen, $\gamma \cdot \Delta B_0$ is the inhomogeneity of the static field in unit, KHz.

From the Eq. [2] and Eq. [3], we can see that in order to determine the inhomogeneity of magnetic field, a sample with the property that T_2^* « $T_{2,b}$ must be used. The pure water (deionized), which has a $T_{2,b}$ relaxation time of 2.9 sec, serves this purpose well. Then, the inhomogeneity $\gamma \cdot \Delta B_0$ of the applied magnetic field in this work can be estimated, which is 0.2128 KHz as shown in Fig. 4.

Due to the high viscosity of bitumen, the $T_{2,b}$ of bitumen is small and comparable to the inhomogeneity of magnetic field. Therefore, both of the two terms on the right side of Eq. [3] count for the single exponential fitting. Given the inhomogeneity obtained from the FID of pure water (Fig. 4), the estimated T_2 of bitumen is 0.518 msec.

3.3 Improved Interpretation Method for Correcting T_2 of Bitumen

Incorporating with the improved experimental scheme described in section 3.2, a new interpretation method was also developed for interpreting the CPMG raw data of bitumen sample. In this new method, the initial magnetization of bitumen sample, which was obtained from FID measurement, was supplemented to the regular CPMG raw data. Then, instead of the standard multi-exponential model, a lognormal distribution model was assumed to represent the T_2 distribution of bitumen part. The derivation of this lognormal distribution based model is shown as below:

The multi-exponential model is expressed by Eq. [1]. Since it consists of two parts, bitumen and water, it can also be expressed as Eq. [4]:

$$M(t) = M_b(t) + M_w(t) = \sum_j f_{b,j} \cdot e^{-\frac{t}{T_{2,j}}} + \sum_k f_{w,k} \cdot e^{-\frac{t}{T_{2,k}}} \quad (4)$$

On the right side of Eq. [4], the first term is for bitumen and the second term is for water part in the bitumen sample. Here, we assume the interpretation for water part is correct from standard multi-exponential model and replace the bitumen part in Eq. [4] with a lognormal distribution model. Then, the $M_b(t)$ in Eq. [4] becomes:

$$M_b(t) = f_{b,0} \sum_j g_{b,j} \cdot e^{-\frac{t}{T_{2,j}}} \quad (5)$$

In Eq. [5], g_j follows lognormal distribution, as shown in Eq. [6]:

$$g_{b,j} = \frac{1}{\sigma\sqrt{2\pi}} \cdot e^{-\frac{[\ln(T_{2,j})-\mu]^2}{2\sigma^2}} \cdot \Delta \ln(T_{2,j}) \quad (6)$$

Where $\sum_{j=1}^{\infty} g_{b,j} \to 1$ (7)

It's clear that, in this lognormal distribution model, there are two unknowns, the log mean T_2 of bitumen, μ, and the standard deviation, σ. In order to optimize the fitting computation, the $\ln(T_{2,j})$ was chosen at μ, $\mu \pm \sigma/2$, $\mu \pm \sigma$, $\mu \pm 3\sigma/2$, $\mu \pm 2\sigma$, $\mu \pm 5\sigma/2$. Then, the T_2 distribution of bitumen could be represented by using eleven points with a lognormal distribution. Thus, in Eq. [6]:

$$\Delta \ln(T_{2,j}) = \frac{\sigma}{2} \tag{8}$$

Here, we assume that only bitumen and water in the bitumen sample give NMR response. Therefore, the total response of bitumen $f_{b,0}$ is equal to the difference between the initial magnetization M_0 of bitumen sample and the total NMR response of water part. Then, the $f_{b,0}$ in Eq. [5] can be expressed as:

$$f_{b,0} = M_0 - \sum_k f_{w,k} \tag{9}$$

Finally, the new model, which combines the original multi-exponential model for water part and a lognormal distribution model for bitumen part, can be expressed as below:

$$M(t) = f_{b,0} \sum_j g_{b,j} \cdot e^{-\frac{t}{T_{2,j}}} + \sum_k f_{w,k} \cdot e^{-\frac{t}{T_{2,k}}} \tag{10}$$

3.4 Interpretation of CPMG Raw Data at 30 °C with New Model

The M_0 obtained from the FID supplemented the CPMG data. The newly developed model as shown by Eq. [10] was employed to fit the augmented CPMG data at 30 °C.

The fitting results for the CPMG signal obtained with three different echo spacing are shown in Fig. 5. The zoom-in for the first 10 msec in Fig. 5, which is mainly from the decay of bitumen part, is shown in Fig. 6. From Fig. 5 and Fig. 6, we can find that the new model fit the CPMG raw data of bitumen very well. The interpretations of CPMG data are shown in Fig. 7. The T_2 distributions of bitumen sample obtained from the standard multi-exponential model without specified M_0 are compared with the results from the new model.

As shown in the cumulative T_2 distribution in Fig. 7, the area of the bitumen peak is significantly increased by using the new interpretation method. This is due to the compensation for the loss of T_2 information shorter than echo spacing in regular CPMG measurements. The estimated values for the T_2 of bitumen from the two different methods are displayed in Fig. 8.

As displayed in Fig. 7 and Fig. 8, the T_2 of bitumen estimated by specifying M_0 in CPMG data and assuming lognormal distribution for bitumen are remarkably shorter than corresponding T_2 obtained from the regular CPMG

interpretation. More importantly, the corrected T_2 of bitumen has little dependence on echo spacing and is close to the T_2 estimated from FID.

3.5 Application at Different Sample Temperature

It is well known that the temperature of the environment for well logging varies with each application. Therefore, after the successful application in 30 ^{o}C case, this new method was also applied for the measurements at different sample temperatures. The temperature range in this work is from 8 ^{o}C to 90 ^{o}C, which is adequate for the Canadian bitumen logging. Some important properties of bitumen at different temperatures were evaluated by using its T_2 obtained from the new method.

3.5.1 Theoretical Basis for Variation of M_0 with Temperature

The change of initial magnetization in magnetic field with temperature is governed by Curie's Law [14], which can be expressed as Eq. [11]:

$$M_0 = \frac{N\gamma^2\hbar^2 I(I+1)}{3kT} H_0 \tag{11}$$

Where,

N , number of spins;

γ , gyromagnetic ratio;

$\hbar$, Planck's constant / 2π;

I , nuclear spin quantum number;

H_0 , magnetic field;

According to Curie's Law, when the temperature increases, the initial magnetization, M_0 should decrease. In this work, for a given sample system, each parameter shown on the right side is constant except for the temperature. Thus, Eq. [11] can be reduced to:

$$M_0 = \frac{Const}{T} \tag{12}$$

Here, the term $Const$ in above equation is a certain constant for a given sample system.

3.5.2 Calculation of *HI* and Saturation at Different Temperatures

The hydrogen index (*HI*) of a fluid is defined as the proton density of the fluid at any given temperature and pressure divided by the proton density of pure water in standard conditions. It can be expressed as below [15]:

$$HI = \frac{\text{Amount of Hydrogen in Sample}}{\text{Amount of Hydrogen in an equal volume of Pure Water}} \quad (13)$$

The hydrogen index should be a quantity independent of measurement methods. In this work, the hydrogen index of bitumen can be expressed as Eq. [14].

$$HI_b = \frac{\left(\sum f_{b/b+w} / V_{b/b+w}\right)_{\text{at conditions of interest}}}{\left(T_{\text{standard}} / T_{\text{interest}}\right) \cdot \left(M_{0,w} / V_t\right)_{\text{at standard condition}}} \quad (14)$$

Here,

$\sum f_{b/b+w}$, sum of *f* of bitumen part in the bitumen sample;

$\sum f_{w/b+w}$, sum of *f* of water part in the bitumen sample;

$M_{0,w}$, initial magnetization of pure water;

$V_{b/b+w}$, volume of bitumen part in the bitumen sample;

$V_{w/b+w}$, volume of water part in the bitumen sample;

V_t , total volume of bitumen sample and volume of pure water standard;

T_{standard} , standard temperature of pure water sample;

T_{interest} , interested temperature of pure water sample;

In this work, the total volume of bitumen sample is equal to the volume of pure water as standard, thus the volume of water in the bitumen sample can be estimated by Eq. [15] as below:

$$V_{w/b+w} = V_t \cdot \frac{\left(\sum f_{w/b+w}\right)_{\text{at conditions of interest}}}{\left(T_{\text{standard}} / T_{\text{interest}}\right) \cdot \left(M_{0,w}\right)_{\text{at standard condition}}} \quad (15)$$

Then, the volume of bitumen in sample can obtained from the volume difference between the total sample and the water in bitumen sample,

$$V_{b/b+w} = V_t - V_{w/b+w} \quad (16)$$

Another assumption, which was necessary for the investigation on bitumen sample at different temperature, is that the difference of sample volume within our interested temperature range is negligible. Consequently, Eq. [14] becomes,

$$HI_b = \frac{\dfrac{\sum f_{b/b+w}}{1 - \left(\sum f_{w/b+w} / M_{0,w}\right)_{\text{at conditions of interest}}}}{\left(T_{\text{standard}} / T_{\text{interest}}\right) \cdot \left(M_{0,w} / V_t\right)_{\text{at standard condition}}} \quad (17)$$

The equation for calculating water saturation S_w can be derived from Eq. [15] and expressed as:

$$S_w = \frac{V_{w/b+w}}{V_t} = \frac{\left(\sum f_{w/b+w}\right)_{\text{at conditions of interest}}}{\left(T_{\text{standard}} / T_{\text{interest}}\right) \cdot \left(M_{0,w}\right)_{\text{at standard condition}}} \quad (18)$$

3.5.3 Investigation on Bitumen Sample at Different Temperatures

Besides 30 ^{o}C, the bitumen sample was also measured at 8, 20, 40, 50, 60, 70, 80, 90 ^{o}C, respectively. The same interpretation method as used in 30 ^{o}C case was employed. The *HI* and viscosity of bitumen as well as the water saturation in the sample were estimated by using the T_2 of bitumen obtained from the new method.

3.5.3.1 M_0 from FID at Different Temperatures

Fig. 9 displays the initial magnetization of bitumen sample at 8, 20, 30, 40, 50, 60 ^{o}C, which were estimated from extrapolation of FID. According to Curie's law, when temperature increases, the M_0 of sample should decreases correspondingly. However, as shown in Fig. 9, the apparent M_0 extrapolated from FID increases with temperature from 8 to 60 ^{o}C, which is opposite to the theoretical prediction. Moreover, when the temperature is over 40 ^{o}C, the extrapolated M_0 becomes very close to each other (indicated by the arrow). Meanwhile, the FID data is tending to become flatter when the temperature increases, which is indicative of the signal attenuation of FID decreases with increase in temperature.

Fig. 10 displays the initial magnetization of bitumen sample estimated from FID at 60, 70, 80, 90 ^{o}C. It's clear that, when temperature is increased over 60 ^{o}C, the bitumen M_0 starts decreasing as sample temperature increases. This obeys the trend of Curie's Law.

The apparent M_0 of bitumen sample extrapolated from FID at different temperatures are also summarized in Fig. 11. An important observation that can be made from Fig. 11 is that the apparent M_0 increases with temperature when the sample temperature ≤ 60 ^{o}C. As the temperature is raised over 60 ^{o}C, the extrapolated M_0 starts decreasing with temperature, although it does not strictly follow the prediction of Curie's Law.

The following is the explanation to the unexpected results of extrapolated M_0 at temperature ≤ 60 ^{o}C shown in Fig. 9 and Fig. 11. The NMR spectrometer, MARAN 2 used in this work has a 80 □sec dead time before the first FID signal can be collected (as shown in Fig. 9 and Fig. 10). Due to the high viscosity of bitumen, the lost FID signal within the first 80 □sec may attenuate much faster than that within the following part. When the temperature decreases, the viscosity of bitumen increases, resulting in an even faster attenuation of FID signal (indicated by the steeper FID at lower temperature). Then, more FID information of bitumen will be lost within the dead time and possible departure from a straight line has a greater effect upon the extrapolation. Thus, M_0 directly extrapolated from the collected FID data was not accurate for those temperatures ≤ 60 ^{o}C.

This proposed explanation was supported by the results from the measurement with 20 MHz Bruker minispec spectrometer, which had a dead time of 50 □sec rather than the 80 □sec of the 2 MHz Maran-II. Fig. 12 displays the Bruker FID signal measured on the same Athabasca bitumen but smaller sample size at 8 ^{o}C and 20 ^{o}C. As we expected that, the faster attenuations of bitumen FID signal are observed before 80 □sec especially at the lower temperature (8 ^{o}C).

The incorrect temperature dependence of the apparent M_0 at low temperatures (< 60 ^{o}C) can be corrected by the Curie's Law. Given a real M_0 value at certain temperature, the M_0 of the same sample at any other temperatures can be predicted by using Eq. [12]. When the temperature of bitumen is over 60 ^{o}C, the sample viscosity is low enough that complete FID information is assumed to be collected and the extrapolated M_0 decreases with increasing temperature as expected. Therefore, the extrapolated M_0 value at temperature ≥ 60 ^{o}C can be used as the basis for the Curie's Law correction. As shown in Fig. 11, the difference between the 60 ^{o}C-based prediction (solid line) and the 90 ^{o}C-based prediction (dashed line) is 3.2 %. In this work, the 60 ^{o}C-based prediction of M_0 were employed for all the following calculations.

3.5.3.2 Interpretation of CPMG at Different Temperatures

Supplementing the Curie's Law corrected M_0 into the regular CPMG raw data, the experimental data with specified M_0 at each temperature were fitted to the lognormal distribution based model and the fitting results are shown in Fig. 13. The correspondingly interpreted T_2 distribution of bitumen is shown in Fig. 14 (a).

Fig. 14 (b) demonstrates the T_2 distribution of bitumen interpreted by using the apparent M_0. Comparing Fig. 14 (a) and Fig. 14 (b), we can find that the T_2 distributions of bitumen obtained by simply using the apparent M_0, which directly extrapolated from FID, have remarkable difference from those obtained by using Curie's Law corrected M_0. Both peak area and peak position vary when different M_0 is employed during the interpretation. Moreover, the lower the temperature, the larger the difference.

As shown in Fig. 14 that, at sample temperature ≤ 60 ^{o}C, the estimated T_2 of bitumen by using the Currie's Law corrected M_0 are uniformly shorter than those estimated with the extrapolated apparent M_0 at each temperature. When the temperature rises over 60 ^{o}C, the difference between the two T_2 of bitumen becomes very small.

Furthermore, after using the Curie's Law corrected M_0, the area of bitumen peak at temperature ≤ 60 ^{o}C is significantly increased. Also, the NMR responses from bitumen, which is indicated by the bitumen peak area, start following the Curie's Law and decreases with increasing temperature.

3.5.3.3 Estimated Water Saturation in Sample at Different Temperatures

The T_2 distribution of water part in bitumen sample, which was interpreted from the standard multi-exponential model is assumed to be correct. The local minimum after oil peak is employed as the cut-off between oil peak and water response of bitumen sample. In this manner, the water saturation of bitumen sample at each temperature was estimated by using Eq. [18].

As shown in Fig. 15, the estimated S_w suddenly decreases when the temperature ≥ 60 ^oC. The solid horizontal line is the average value of S_w at 8 ~ 50 ^oC and the corresponding percentage standard deviation is 2.5 %.

A proposed explanation to the sudden decrease of S_w at temperature ≥ 60 ^oC is that the cut-off we used in this work to distinguish oil peak and water peaks is not proper in those high temperature cases. When the sample temperature is lower than 60 ^oC, the bitumen peak is clearly separated from the water peaks. We can simply use the local minimum after the bitumen peak as the cut-off. However, when the sample temperature is raised over 60 ^oC, due to the comparable T_2 of emulsified water and bitumen, the water peaks run into the bitumen peak, as shown in Fig. 16. Using the local minimum as the cut-off may not be proper under these conditions.

A more sophisticated oil-water cut-off is necessary in the research on bitumen at high temperatures. In this work, the sample tube was well-sealed. We purposely shuffled the experiment sequence to avoid any unexpected temperature-sequence-dependent results. For example, the 20 ^oC measurement was performed after the 90 ^oC one. Based on the experimental data shown in Fig. 14, it's reasonable to assume that the real water saturation of bitumen sample does not change within the temperature range of this work.

Therefore, we may be able to use the water saturation data at low temperatures (8 ~ 50 ^oC) to calibrate the cut-off at high temperatures (60 ~ 90 ^oC) in the following research. On the other hand, due to the significant difference between the diffusivities of bitumen and water, we may also use Diffusion Editing measurement to evaluate the NMR response of emulsified water in bitumen samples.

3.5.3.4 Estimated *HI* of Bitumen at Different Temperatures

The hydrogen index (*HI*) of bitumen at different temperature can be calculated by using Eq. [17] and the results are shown in Fig. 17. It is clear that, when the extrapolated M_0 from FID is not corrected by Curie's Law, the apparent *HI* of bitumen has an incorrect dependence on temperature. This is due to the incorrect temperature dependence of apparent M_0 (as shown in Fig. 9 and Fig. 11) when sample temperature < 60 ^oC, and the inaccurate cut-off for calculating the water saturation (as shown in Fig. 14 and Fig. 15) at temperature ≥ 60 ^oC.

However, after the correction for M_0, the incorrect temperature dependence is eliminated and the bitumen *HI* stays constant at different temperature. The average value is 0.82 and the percentage standard deviation is only 0.6 %.

3.5.3.5 Estimated Viscosity of Bitumen at Different Temperatures

A correlation of log-mean T_2 with the ratio of viscosity and temperature, which was derived from alkanes T_1, was developed in previous work of our group [7] and [8]. As shown in Fig. 18, given the corrected T_2, the alkane correlation was used to estimate the viscosities of bitumen at different temperatures.

The viscosities of bitumen at elevated temperatures were also measured by Brookfield Viscometer and were used to compare with the NMR based estimations from the alkane correlation shown in Fig. 18.

As displayed in Fig. 19, the viscosity of bitumen estimated from the alkane correlation has significant discrepancy from the experimental value measured by viscometer at low temperatures. As the sample temperature increases, the viscosity of bitumen decreases and the difference between the two viscosity values keeps decreasing. When it reaches 90 ^{o}C, the calculated value becomes equal to the experimental value. This means that the alkane correlation, as many other NMR Relaxation Time vs. Viscosity correlations [3], [4], [6] and [16], is only good for the oil with relatively low viscosity, but not suitable for those with extremely high viscosity like bitumen. In order to find out the reason responsible for the discrepancy, we need to start from the theoretical basis on highly viscous oil relaxation.

Dead crude oils relax mainly by intramolecular dipole-dipole interactions [17]. The intramolecular dipole-dipole interaction mechanism is due to the interaction of nuclei in the same molecule. If the molecule is regarded as rigid, the relaxation results from the rotational motion of the molecule [18]. For spherical molecules, the relaxation times by the intramolecular dipole-dipole interaction are expressed as [18]:

$$\frac{1}{T_1} = W_2 \tau_c \left[\frac{2/3}{1+(\omega_0 \tau_c)^2} + \frac{8/3}{1+(2\omega_0 \tau_c)^2} \right], \tag{19}$$

$$\frac{1}{T_2} = W_2 \tau_c \left[1 + \frac{5/3}{1+(\omega_0 \tau_c)^2} + \frac{2/3}{1+(2\omega_0 \tau_c)^2} \right], \tag{20}$$

$$W_2 = \frac{3(\nu-1)\gamma^4 \hbar^2 I(I+1)}{5r^6}, \tag{21}$$

where ω_0 is the Larmor frequency, and τ_c is the rotational correlation time.

In the fast motion case (the extreme narrowing limit), Eq. [19] and Eq. [20] reduces to

$$\frac{1}{T_1} = \frac{1}{T_2} = \frac{10}{3} W_2 \tau_c , \quad \omega_0 \tau_c \le 1. \tag{22}$$

The rotational correlation time can be related to measurable variables through the rotational diffusion coefficient D_r. For spherical molecules, the rotational correlation time is given by [19]:

$$\tau_c = \frac{1}{6D_r} = \frac{4\pi a^3 \eta}{3kT} . \tag{23}$$

The substitution of Eq. [23] into Eq. [22] yields

$$\frac{1}{T_1} = \frac{1}{T_2} = \frac{40 W_2 \pi a^3 \eta}{9kT} , \quad \omega_0 \tau_c \le 1. \tag{24}$$

Here we normalized the relaxation time, viscosity and viscosity/temperature ratio with respect to 2 MHz as shown in Eq. [25] and Eq. [26]:

$$T_{1,2N} = \frac{2}{\omega_0} T_{1,2} , \tag{25}$$

$$\eta_N = \frac{\omega_0}{2} \eta . \tag{26}$$

$$\left(\frac{\eta}{T}\right)_N = \frac{\omega_0}{2} \left(\frac{\eta}{T}\right). \tag{27}$$

Combining Eq. [19], Eq. [20], Eq. [23], Eq. [25] and Eq. [27], we have

$$\frac{1}{T_{1N}} = \frac{W_2 S}{2} \left(\frac{\eta}{T}\right)_N \left\{ \frac{2/3}{1+\left[S\left(\frac{\eta}{T}\right)_N\right]^2} + \frac{8/3}{1+\left[2S\left(\frac{\eta}{T}\right)_N\right]^2} \right\}, \tag{28}$$

$$\frac{1}{T_{2N}} = \frac{W_2 S}{2} \left(\frac{\eta}{T}\right)_N \left\{ 1 + \frac{5/3}{1+\left[S\left(\frac{\eta}{T}\right)_N\right]^2} + \frac{2/3}{1+\left[2S\left(\frac{\eta}{T}\right)_N\right]^2} \right\}, \tag{29}$$

$$S = \frac{8\pi a^3}{3k} . \tag{30}$$

Deriving from Eq. [23], Eq. [27] and Eq. [30], we can find that the product of normalized viscosity/temperature ratio and *S*, as shown in Eq. [28] and Eq. [29], is equal to the product of Larmor frequency and correlation time.

$$S \cdot \left(\frac{\eta}{T} \right)_N = \omega_0 \cdot \tau_c . \tag{31}$$

The relationship between the dimensionless relaxation time and the product of Lamor frequency and correlation time is shown in Fig. 20 [8]. An important result here is that liquids in the fast motion limit have T_1 and T_2 equal to each other and inversely proportional to viscosity/temperature. As it comes to slow molecule motion as in high viscosity oil, where $\omega_0 \tau_c \geq 1$, T_1 turns to be larger than T_2 and the difference keeps becoming larger when the ratio of viscosity and temperature is further increased. When the T_1 stops decreasing with $\omega_0 \tau_c$ and starts going up, the T_2 begins to depart from linear relationship on log-log plot.

The experimental results between normalized T_1 or T_2 relaxation times and normalized viscosity/temperature ratio are shown in Fig. 21. Also, some literature data are included on the plot [5], [14], [20] and [21]. The 20 MHz data of bitumen in Fig. 21 were obtained from the measurements by using the 20 MHz Bruker minispec NMR spectrometer. The magnet was operating at 40 ^{o}C for all experiments and a shorter TE (0.184 msec) was employed for the CPMG. The experimental procedure was the same as that used for 2 MHz Maran-II.

As shown in Fig. 21, the frequency-normalized T_1 data of bitumen from this work fall on the same plateau for different Larmor frequencies and follow the curve shown by other literature data. Comparing Fig. 20 and Fig. 21, we can find that the measured T_1 for viscous samples shown in Fig. 21 do not follow the predicted theoretical trend displayed in Fig. 20. Instead of rising up, T_1 levels off at high viscosity and reaches a plateau for normalized viscosity/temperature greater than 1 cP/K.

The experimental T_2 continues to shorten with increasing viscosity. Moreover, T_2 is considerably less than T_1 in all cases for heavy oils. As shown in Fig. 21, the measured bitumen normalized T_2 at either Larmor frequency in this work follows the trend of previous literature data. The black solid line in Fig. 21 is from the T_2 correlation by Morriss et al. [4] and the dashed line is from the Alkane correlation [8]. Although the viscosity predictions from the two correlations have difference for light oils, they are quite similar at high viscosities. Viscosity prediction is adaptable for relatively low viscosity crude oils. However, highly viscous samples significantly depart from both of two correlations.

The correlation derived from the intramolecular dipole-dipole interactions model (expressed by Eq. [29]) was also employed to fit the experimental data. The only variable in Eq. [29] is S and its estimated value in this case is 0.082. The fitting results are plotted as the green solid line in Fig. 21. It is clear that the experimental data of heavy oils also have great departure from the dipole-dipole correlation.

In this manner, further work is undergoing and a new correlation will be developed to better correlate T_2 relaxation time and heavy oil viscosity.

4 Conclusions

1. The echo spacing restriction of regular CPMG measurement on highly viscous bitumen can be overcome by specifying the M_0 in CPMG raw data and assuming lognormal distribution for bitumen during the interpretation.

2. Apparent M_0 of bitumen from FID at low temperatures (< 60 ^{o}C) has incorrect dependence on temperature due to the loss of FID signal within the initial decay period. This incorrect temperature dependence can be corrected by the Curie's Law. Given a correct M_0 value at certain temperature, the M_0 of the same sample at any other temperatures can be predicted by using the equation of Curie's Law.

3. Given Curie's Law corrected M_0 and proper cut-off between oil and water, the hydrogen index (*HI*) and water saturation (S_w) of bitumen sample can be evaluated by using the method in this work. The estimated *HI* of Athabasca bitumen is 0.82.

4. The T_1 and T_2 of Athabasca bitumen follow the trend of previous literature data. Existing T_2 vs. viscosity correlations, which are good for the oil with relatively low viscosity, are not suitable for the samples with extremely high viscosity like Canadian bitumen.

Acknowledgement

The authors gratefully acknowledge the financial support of NSF, USDOE, and the industrial consortium on Processes in Porous Media at Rice University. The advice of Harold Vinegar is gratefully acknowledged. Zvi Taicher is acknowledged for his use of 20 MHz Bruker spectrometer.

References

[1] J.E. Galford, Combining NMR and conventional Logs to Determine Fluid Volumes and Oil Viscosity in Heavy-Oil Reservoirs, Paper SPE 63257, Society of Petroleum Engineers, presented at the 2000 SPE Annual Technical Conference and Exhibition, Dallas, TX, Oct. 1-4, 2000.

[2] M. Deleersnyder, In-Situ Heavy-Oils Viscosity Determination Using NMR and Conventional Logs: Application to a Real Example, Paper SPE 86939, Society of Petroleum Engineers, presented at the SPE International Thermal Operations and Heavy Oil Symposium and Western Regional Meeting, Bakersfield, CA, Mar. 16-18, 2004.

[3] R. Kleinberg, H.J. Vinegar, NMR Properties of Reservoir Fluids, The Log Analyst., 37 (1996) 20-32.

[4] C.E. Morriss, R. Freedman, C. Straley, M. Johnston, H.J. Vinegar, P.N. Tutunjian, Hydrocarbon Saturation and Viscosity Estimation from NMR Logging in the Belridge Diatomite, The Log Analyst, 38 (1997) 44-59.

[5] G.A. LaTorraca, K.J. Dunn, P.R. Webber, R.M. Carlson, Low-Field NMR Determinations of the Properties of Heavy Oils and Water-in-Oil Emulsions, Mag. Res. Imag., 16 (1998) 659-662.

[6] G.A. LaTorraca, S.W. Stonard, P.R. Webber, R.M. Carlson, K.J. Dunn, Heavy Oil Viscosity Determination using NMR Logs, paper PPP, presented at the 40th SPWLA Annual Logging Symposium, SPWLA, Oslo, Norway, May 30 – Jun. 3, 1999.

[7] S.W. Lo, G.J. Hirasaki, W.V. House, R. Kobayashi, Mixing Rules and Correlations of NMR Relaxation Time with Viscosity, Diffusivity and Gas/Oil Ratio of Methane/Hydrocarbon Mixtures, SPEJ March (2002) 24-34.

[8] G.J. Hirasaki, S.W. Lo, Y. Zhang, NMR properties of petroleum reservoir fluids, Mag. Res. Imag. 21 (2003) 269-277.

[9] J. Bryan, A. Kantzas, Oil-Viscosity Predictions From Low-Field NMR Measurements, SPE 89070, SPE Reservoir Evaluation & Engineering, 8 (2005) 44-52.

[10] J. Bryan, A. Mai, F. Hum, A. Kantzas, Oil- and Water-Content Measurements in Bitumen Ore and Froth Samples Using Low-Field NMR, SPE 97802, SPE Reservoir Evaluation & Engineering, 9 (2006) 654-663.

[11] J. Bryan, A. Kantzas, R. Badry, J. Emmerson, T. Hancsicsak, In-situ Viscosity of Heavy Oil: Core and Log Calibrations, Paper 2006-116, presented at the 7th Canadian International Petroleum Conference, Alberta, Canada, June 12-15, 2006.

[12] K.J. Dunn, G.A. LaTorraca, J.L. Warner, D.J. Bergman, On the Calculation and Interpretation of NMR Relaxation Time Distributions, SPE 28367, Society of Petroleum Engineers, The 69th SPE Annual Technical Conference and Exhibition, New Orleans, LA, 1994.

[13] G.R. Coates, L. Xiao, M.G. Prammer, NMR Logging: Principles of Applications, Halliburton Energy Service, Houston, 1999.

[14] B. Cowan, Nuclear Magnetic Resonance and Relaxation, Cambridge University Press, Cambridge, 1997.

[15] K.J. Dunn, D.J. Bergman, C.A. Latorraca, Nuclear Magnetic Resonance Petrophysical and Logging Applications, Pergramon, New York, 2002.

[16] C. Straley, D. Rossini, A. Vinegar, P.N. Tutunjian, C.E. Morriss, Core Analysis by Low-Field NMR, The Log Analyst, 38 (1997) 84-94.

[17] Y. Zhang, PhD Thesis, Rice University, Houston, 2002.

[18] J. McConnell, The Theory of Nuclear Magnetic Relaxation in Liquids, Cambridge University Press, Cambridge, 1987.

[19] J. McConnell, Rotational Brownian Motion and Dielectric Theory, Academic Press, New York, 1980.

[20] K.E. MaCann, A. Vinegar, G.J. Hirasaki, NMR Analysis of Crude Oil and Pure Hydrocarbon Fluids, (private communication), 1999.

[21] H.J. Vinegar, P.N. Tutunjian, W.A. Edelstein, P.B. Roemer, Whole Core Analysis by ^{13}C NMR, SPE Formation Evaluation, 1991 183-189.

Table 1. NMR response of bitumen sample in regular CPMG

Echo spacing (TE) (msec)	Σ *f* of bitumen in sample	Σ *f* of water in sample	Σ *f* of total bitumen sample
0.4	69.0	17.1	86.1
0.8	57.1	16.8	73.9
1.2	37.9	16.9	54.8

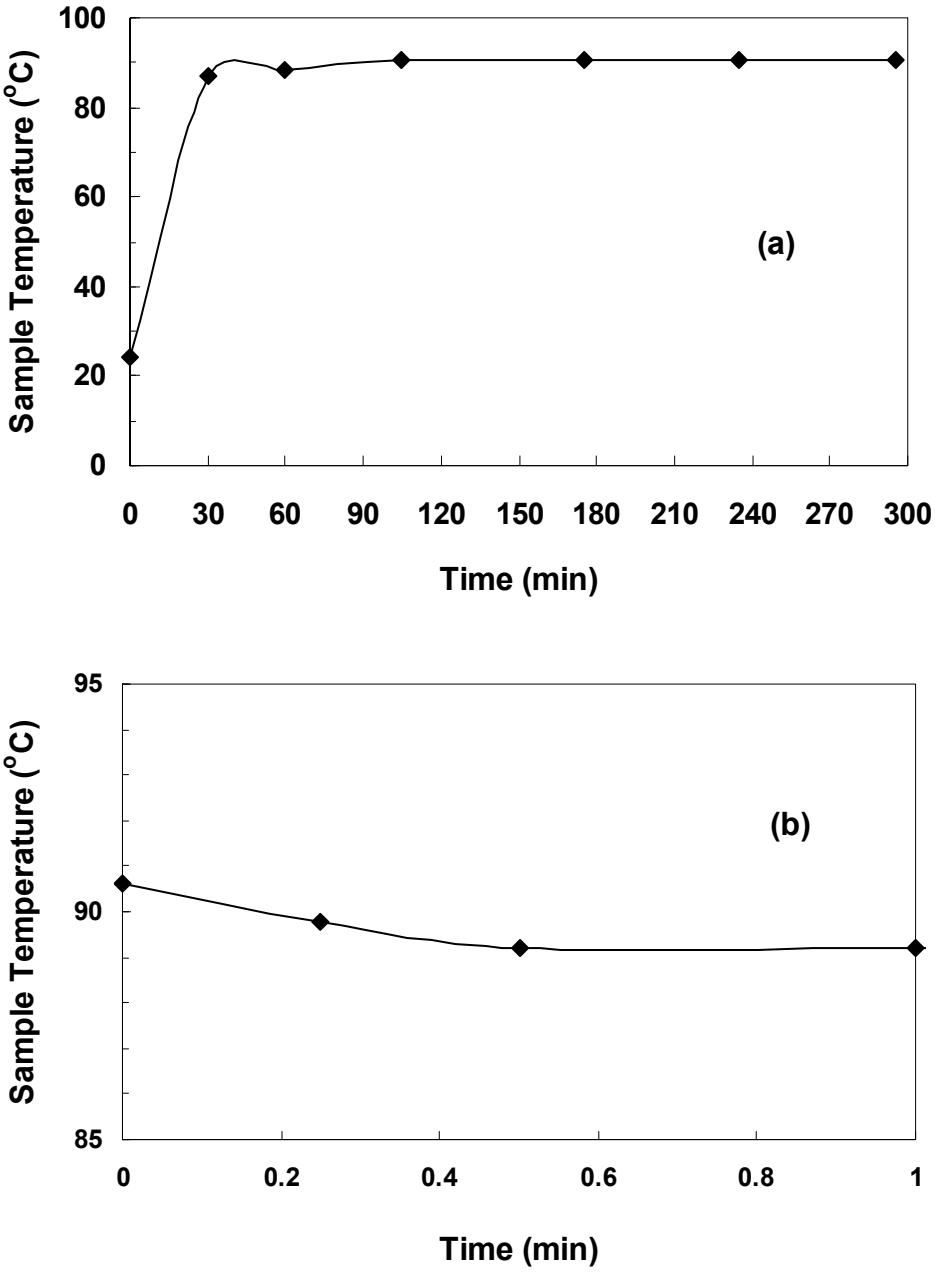

Fig. 1. Temperature change of Athabasca bitumen sample: (a) during heating process, (b) during NMR measurement

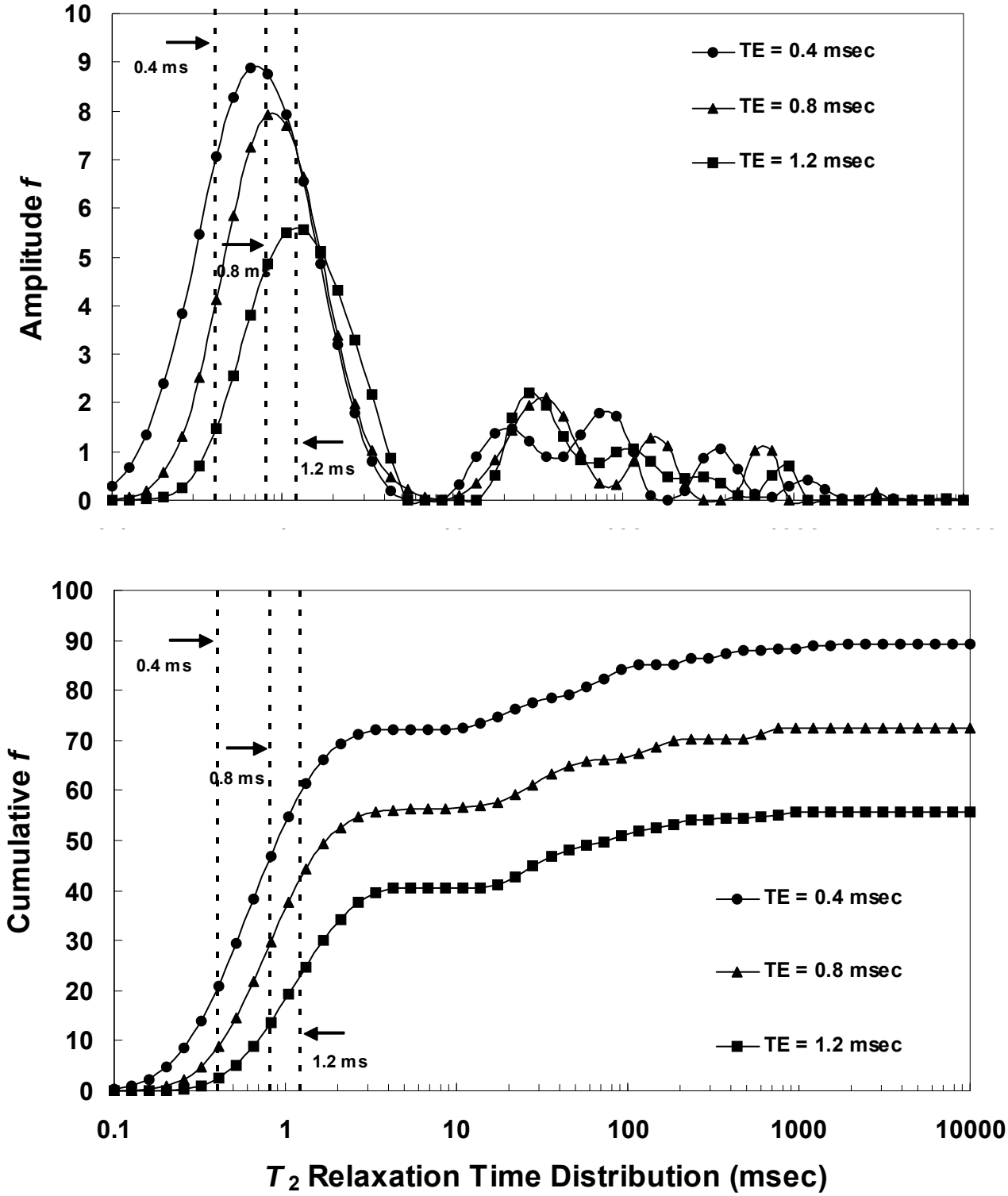

Fig. 2. T_2 distribution of bitumen has strong dependence on echo spacing

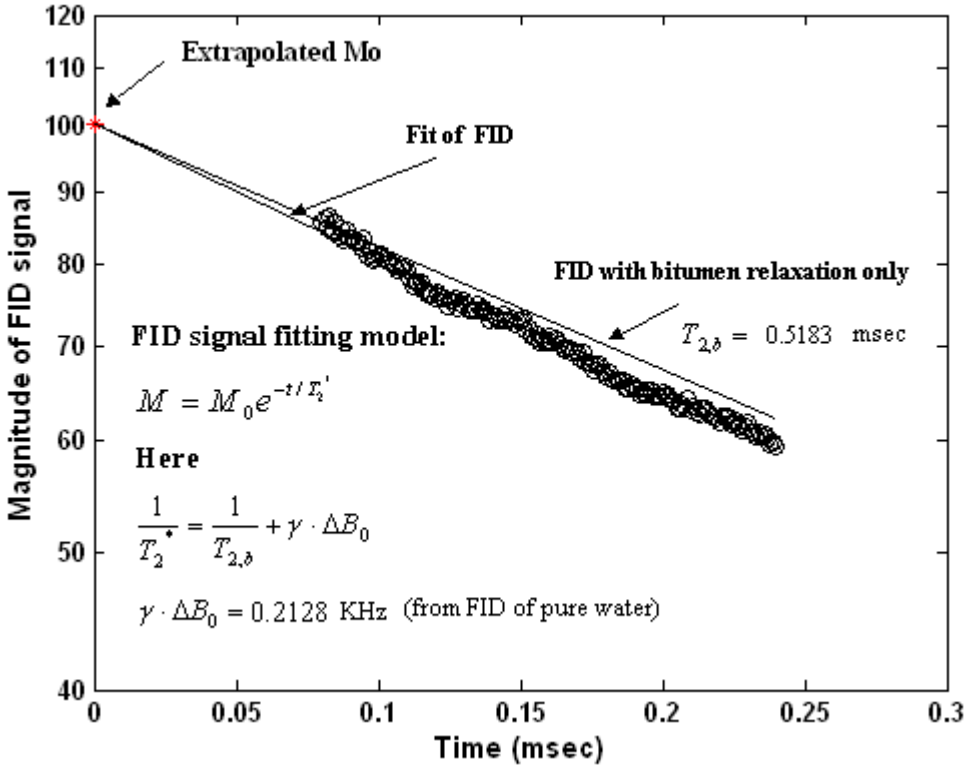

Fig. 3. Extrapolation of FID for M_0, at the start of CPMG

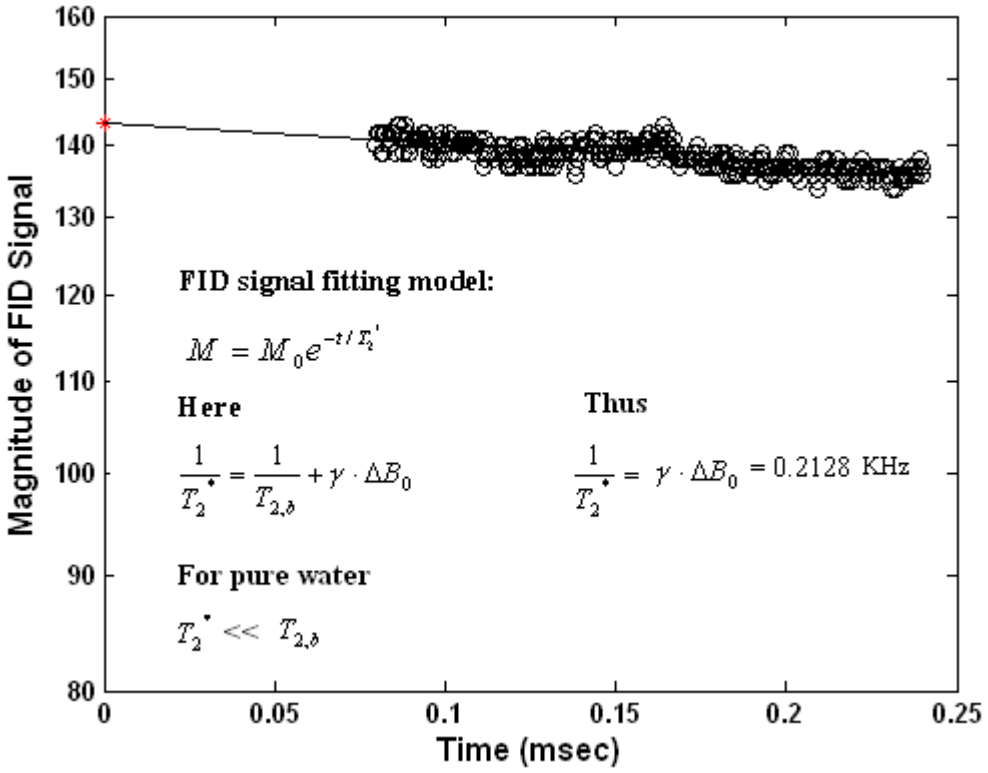

Fig. 4. Estimate inhomogeneity of magnetic field from FID of pure water

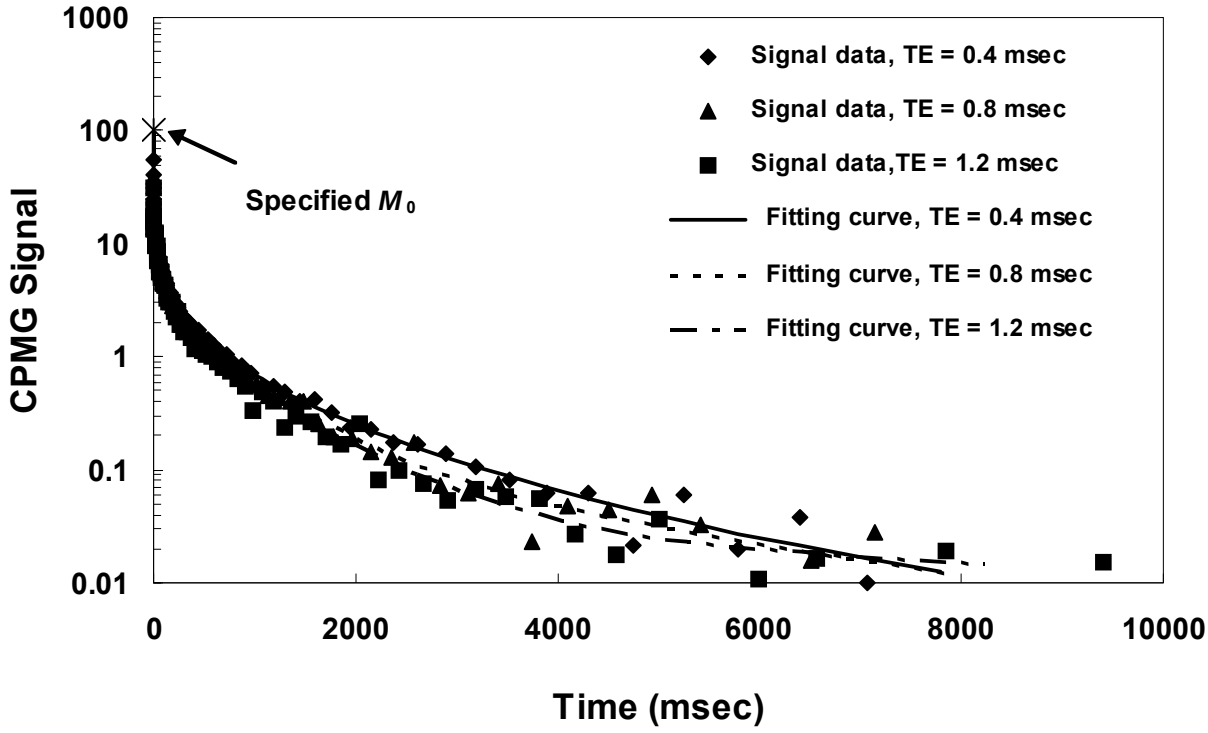

Fig. 5. Fit CPMG data supplemented with M_0 from FID and assume lognormal distribution for bitumen.

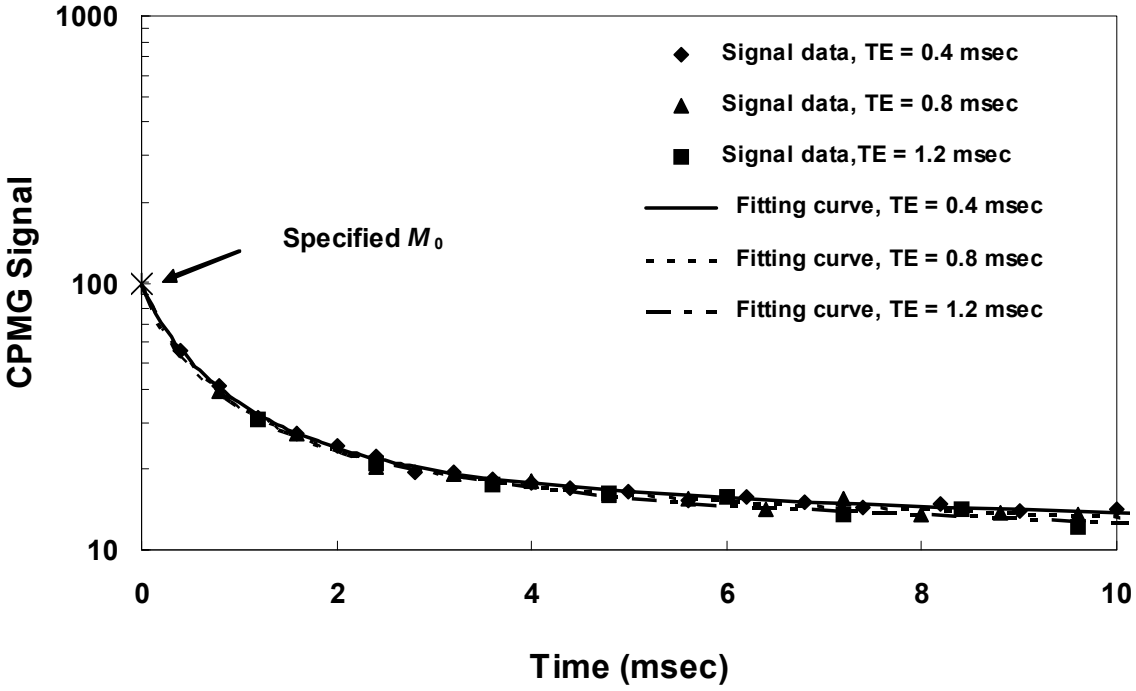

Fig. 6. Zoom-in for the CPMG fitting of first 10 msec in Figure 4

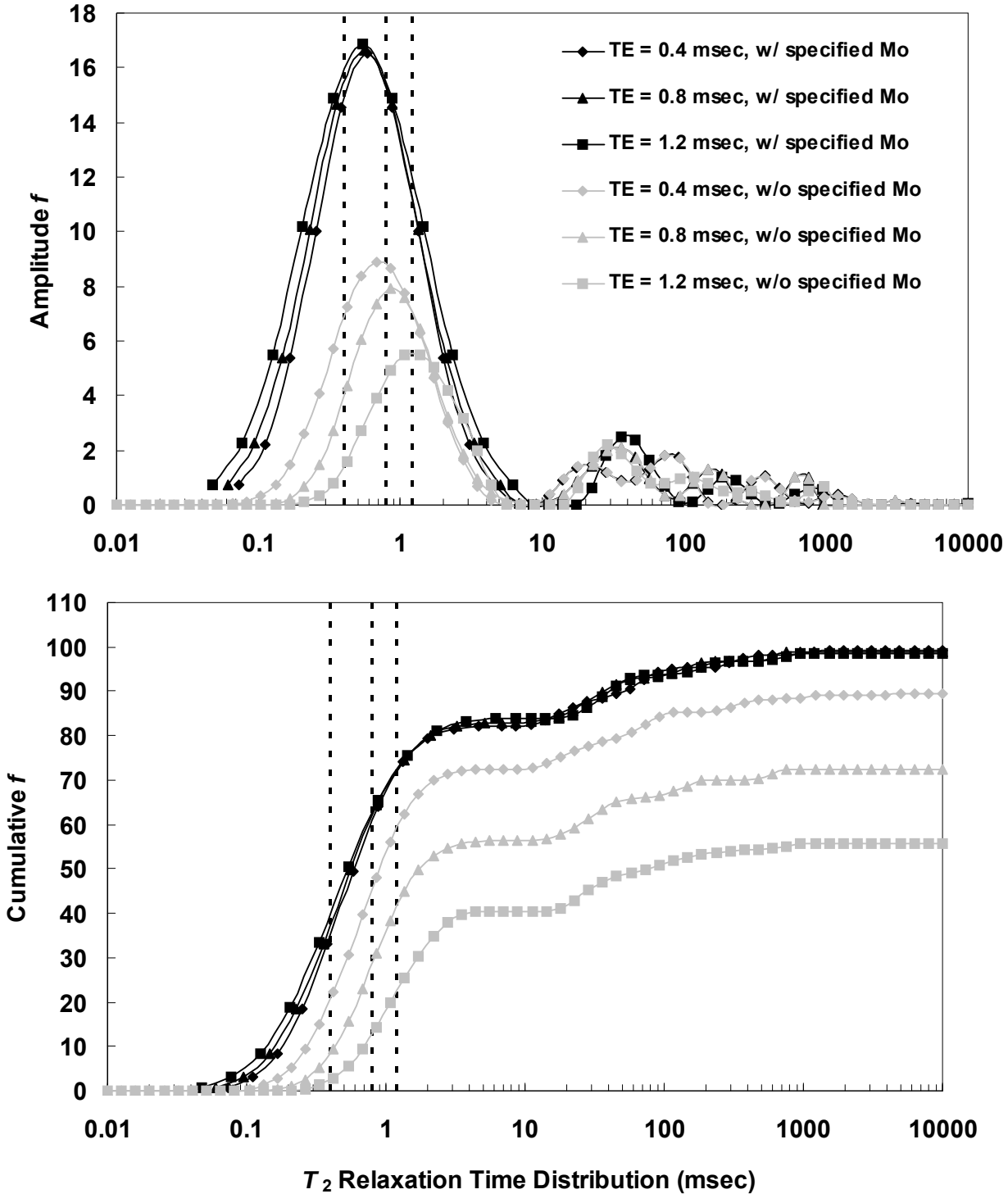

Fig. 7. T_2 distribution of bitumen sample with supplemented M_0 and assuming lognormal distribution for bitumen.

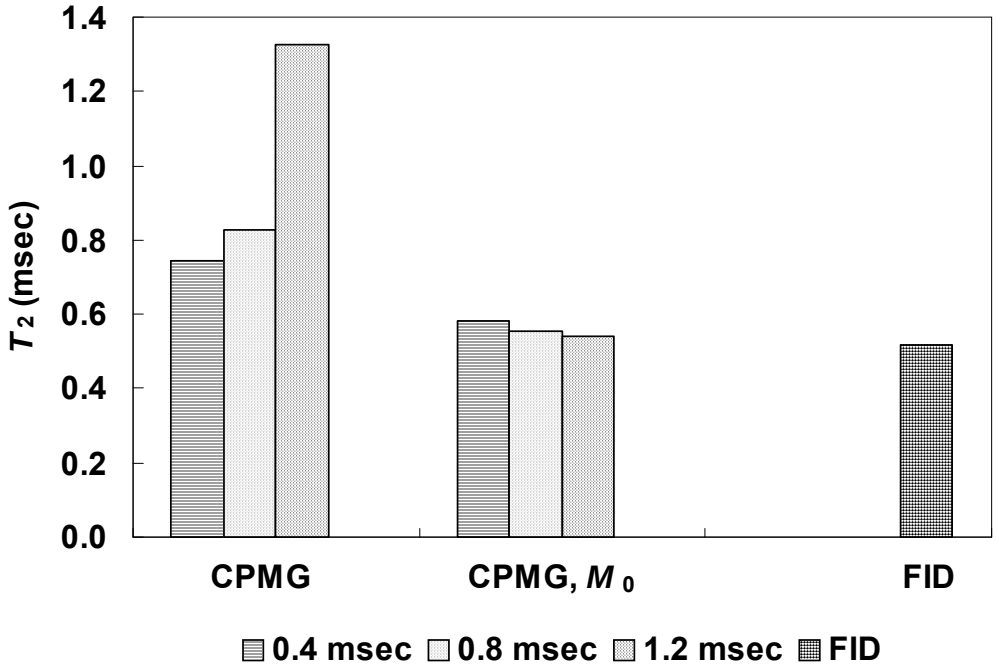

Fig. 8. Estimate T_2 of bitumen from different methods.

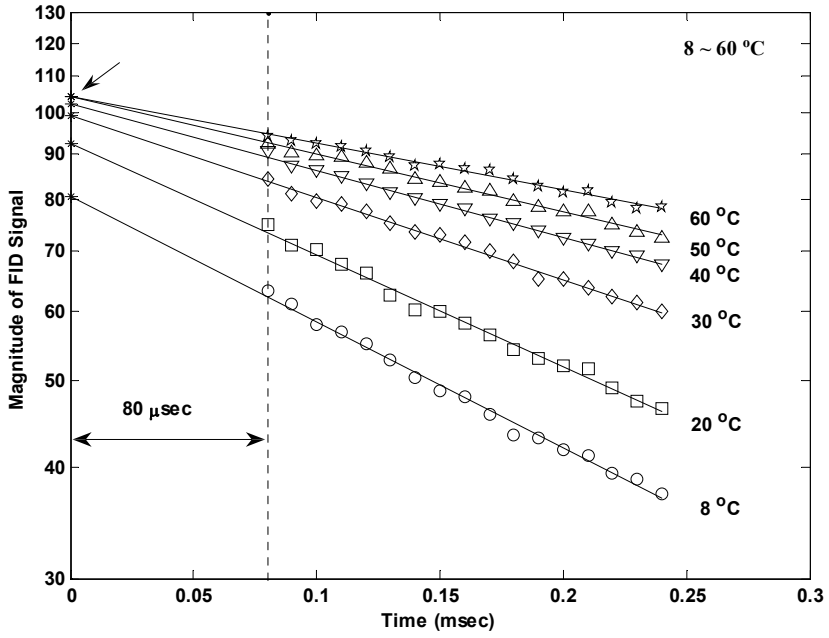

Fig. 9. Extrapolate M_0 of bitumen sample from FID at temperatures: 8 ~ 60 °C

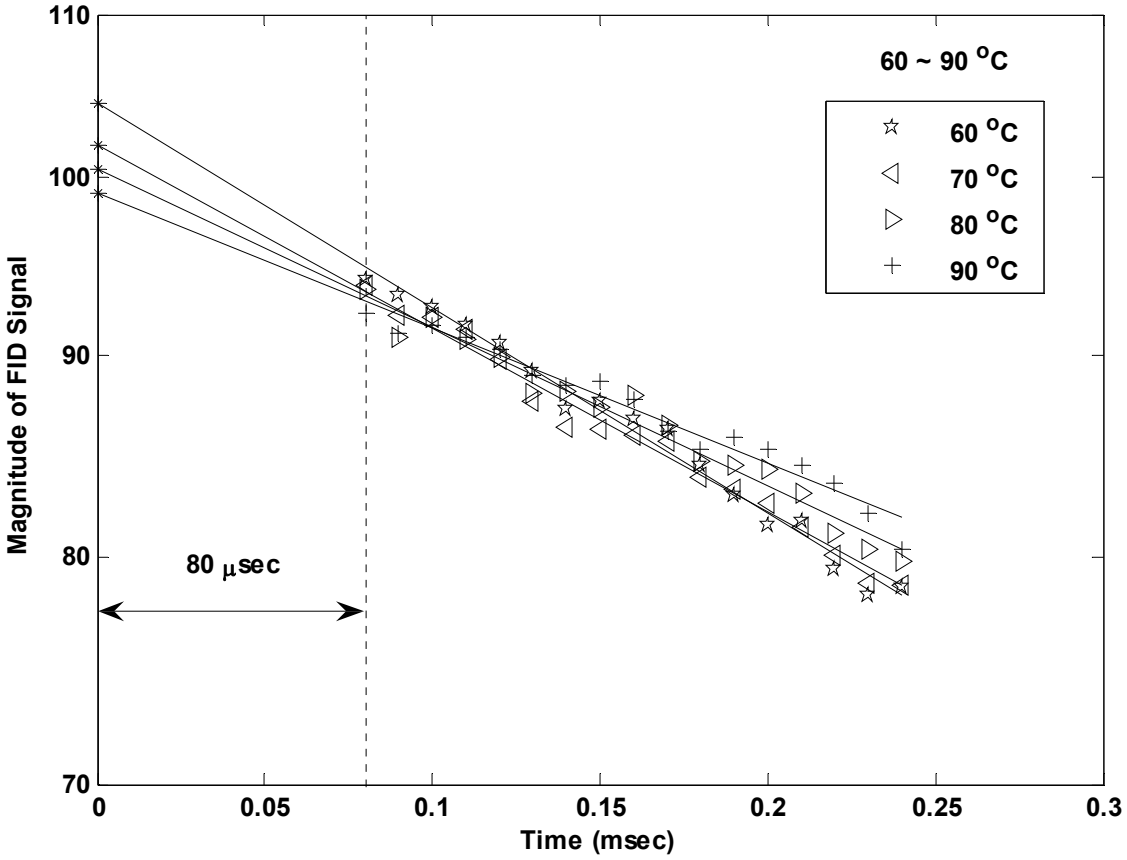

Fig. 10. Extrapolate M_0 of bitumen sample from FID at temperatures: 60 ~ 90 °C

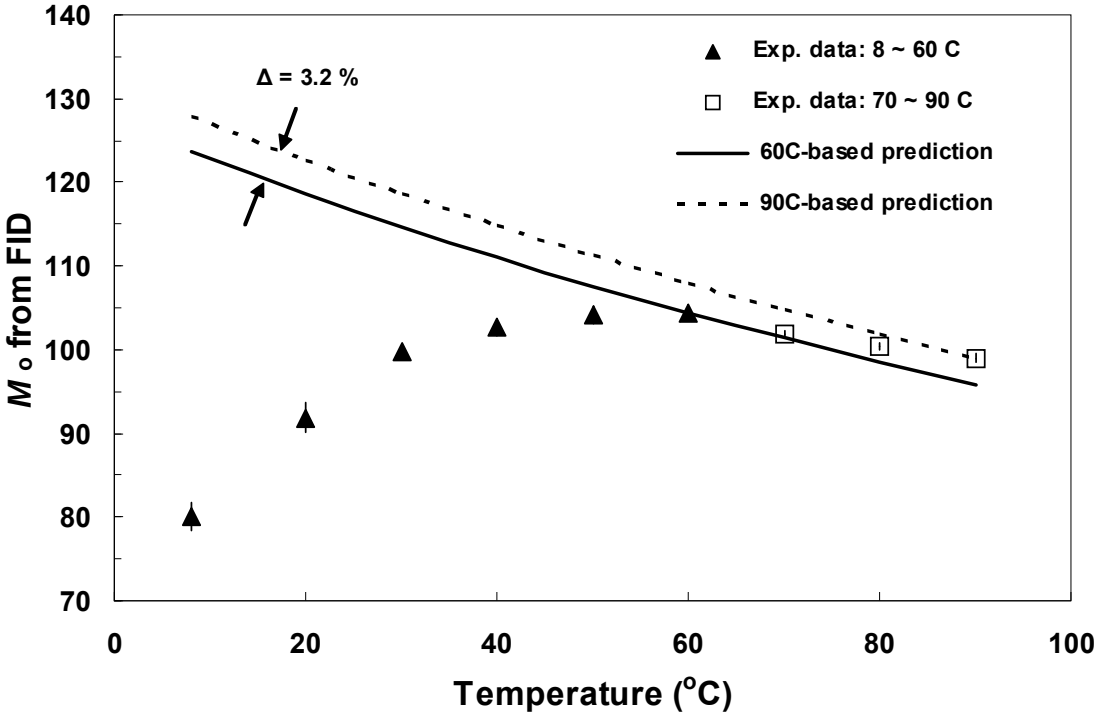

Fig. 11. M_0 of bitumen sample at different temperatures

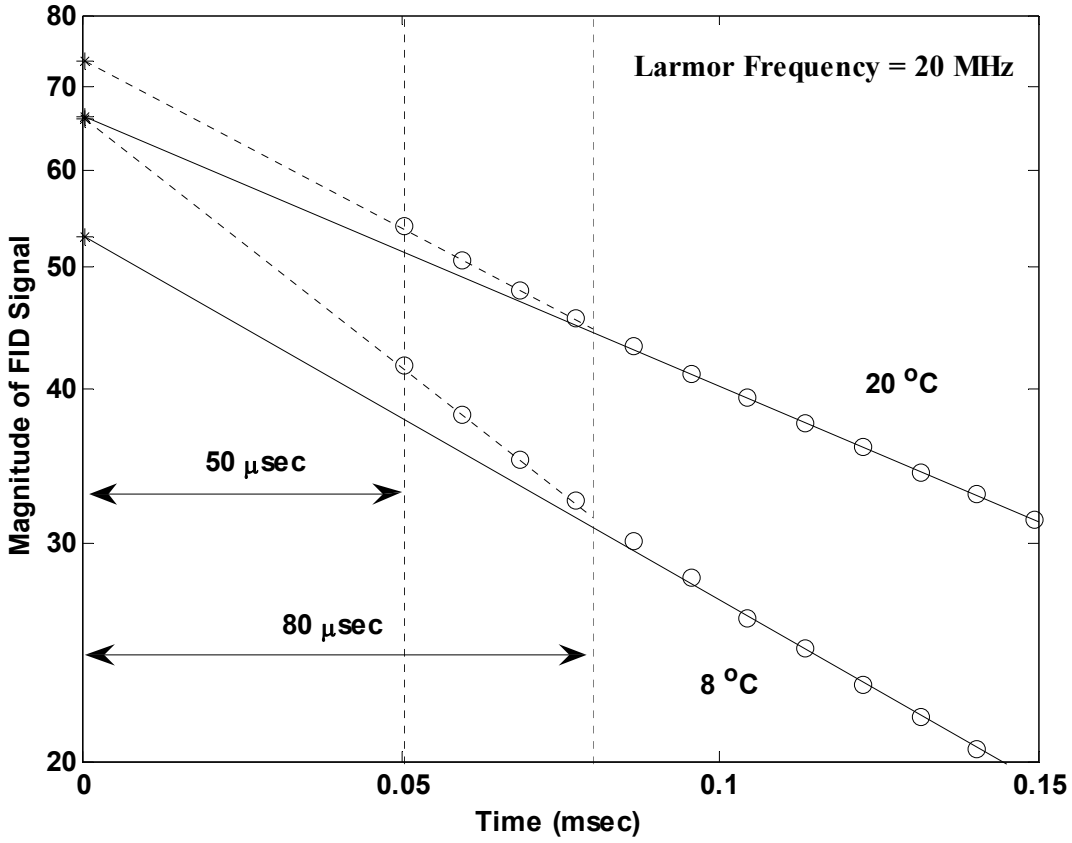

Fig. 12. FID of bitumen sample at 8 °C and 20 °C. Here, the 20 MHz Bruker minispec NMR spectrometer with a dead time of 50 μsec was used. Dashed lines are extrapolation from data 50 ~ 80 μsec. Solid lines are extrapolation from data ≥ 80 μsec.

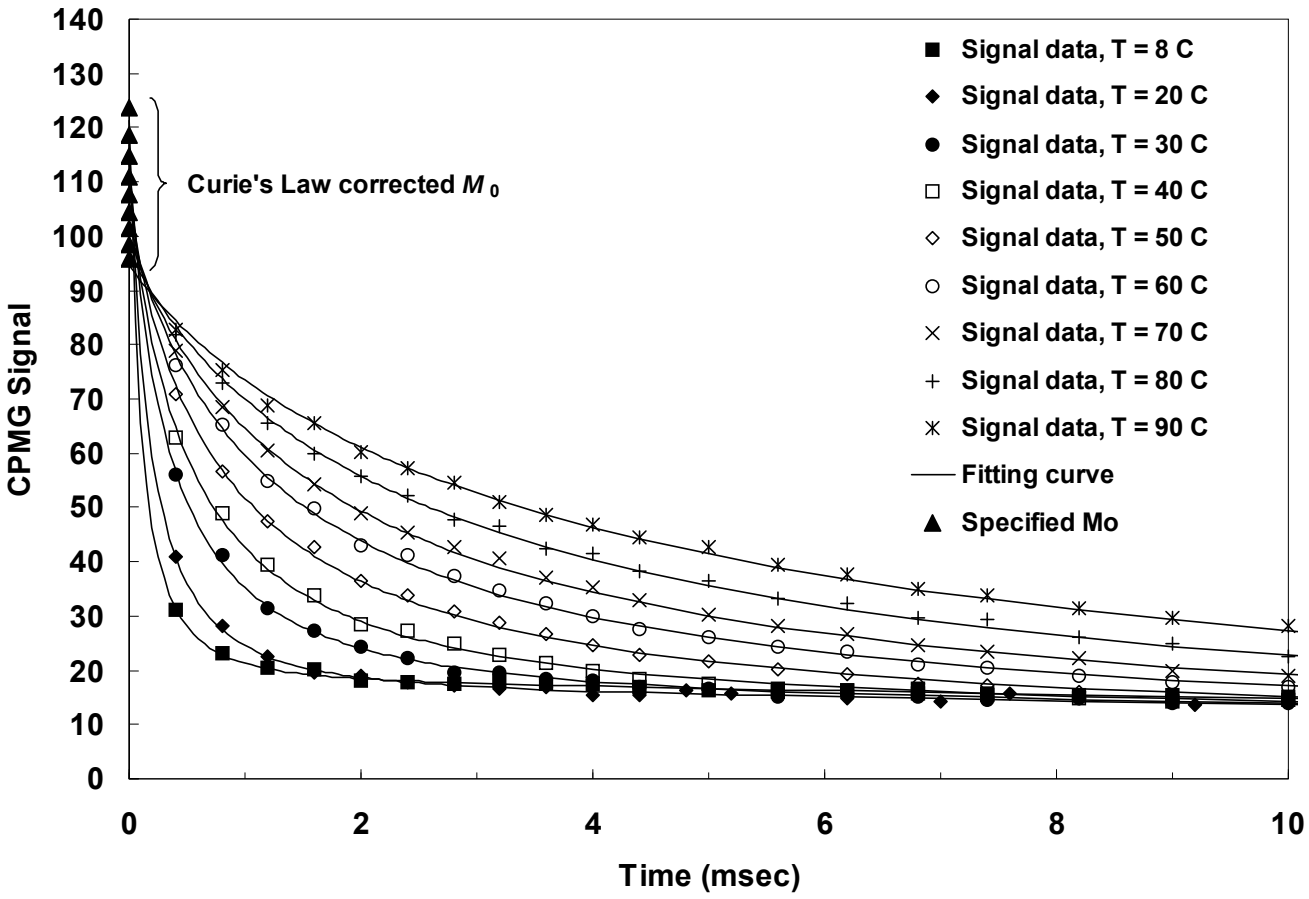

Figure 13. Fitting supplemented CPMG data by assuming lognormal distribution for bitumen. Here, the specified M_0 is corrected by Curie's Law

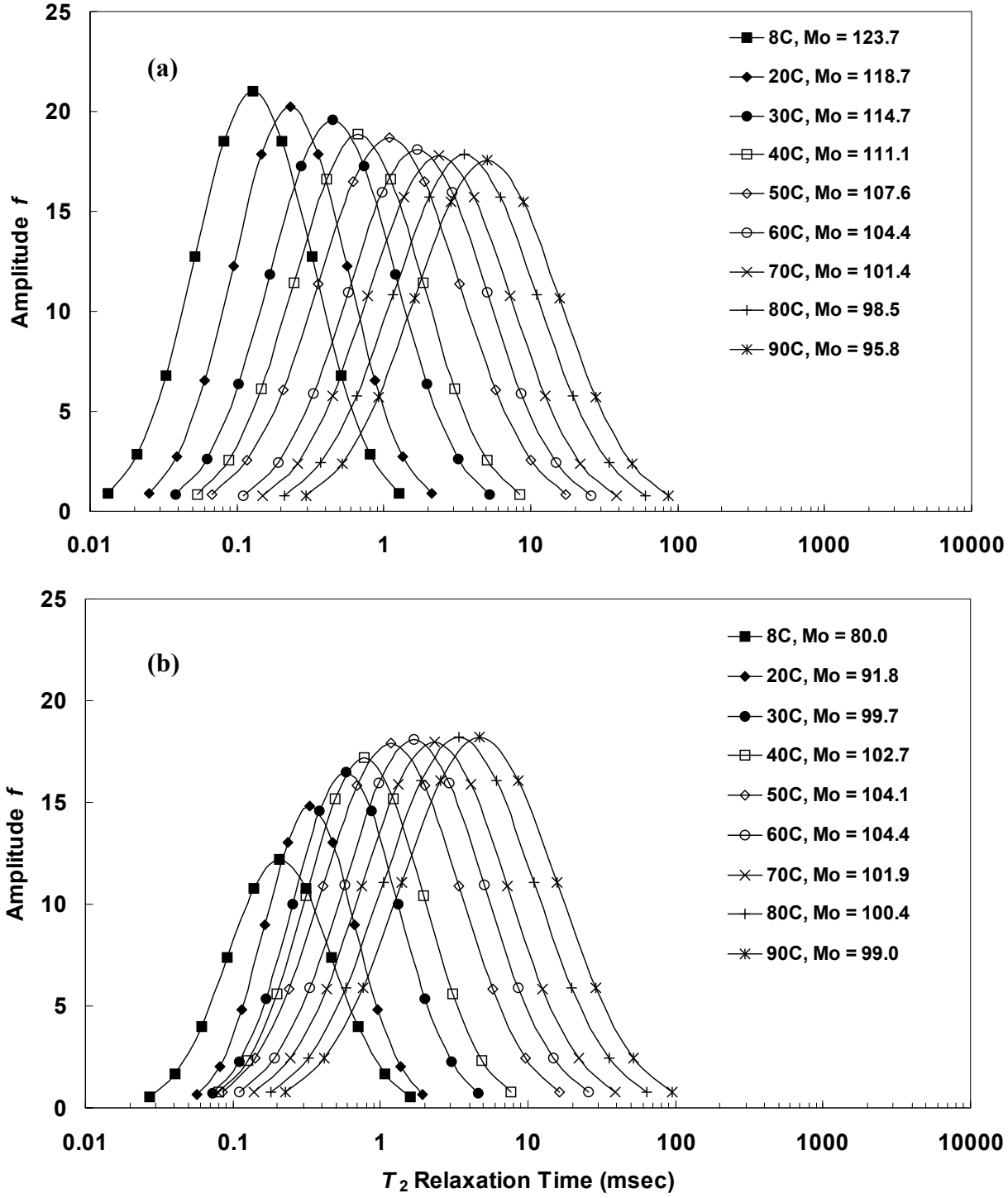

Figure 14. T_2 distribution of bitumen part obtained by assuming lognormal distribution for bitumen part and specifying M_0. Here, (a) is using Curie's Law corrected M_0; (b) is using apparent M_0 without Curie's Law correction.

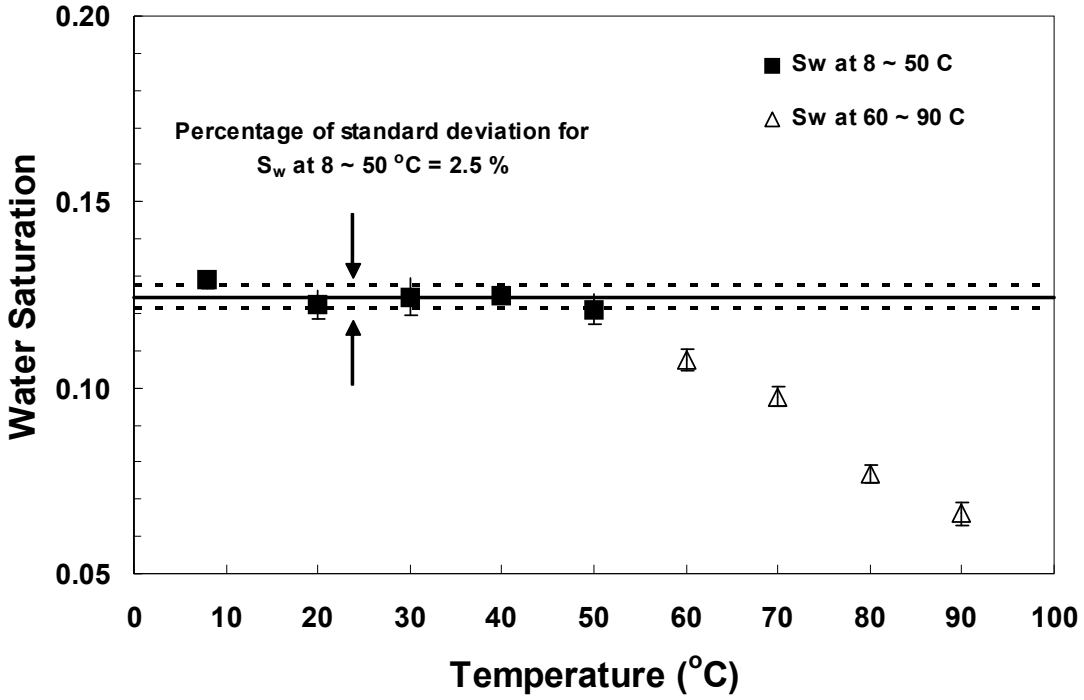

Fig. 15. Estimated water saturation in bitumen sample

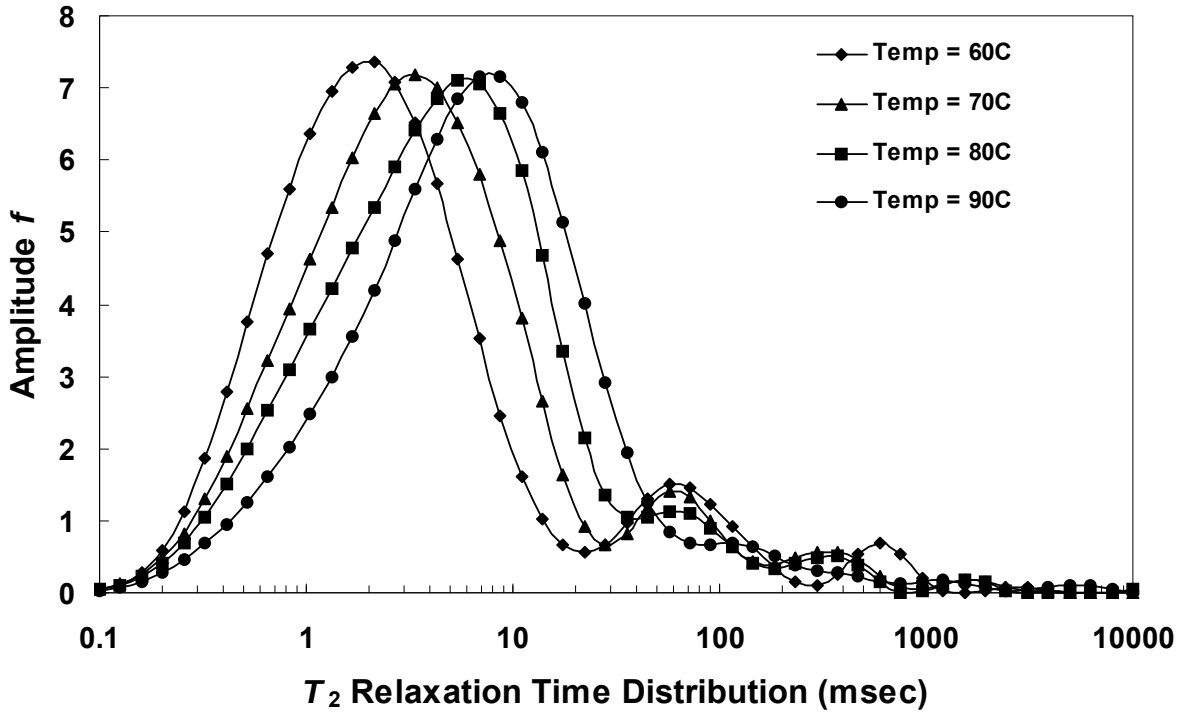

Fig. 16. T_2 distribution of bitumen at temperatures 60, 70, 80, 90 ^{o}C, respectively. Here, the CPMG data were interpreted by using the multi-exponential model.

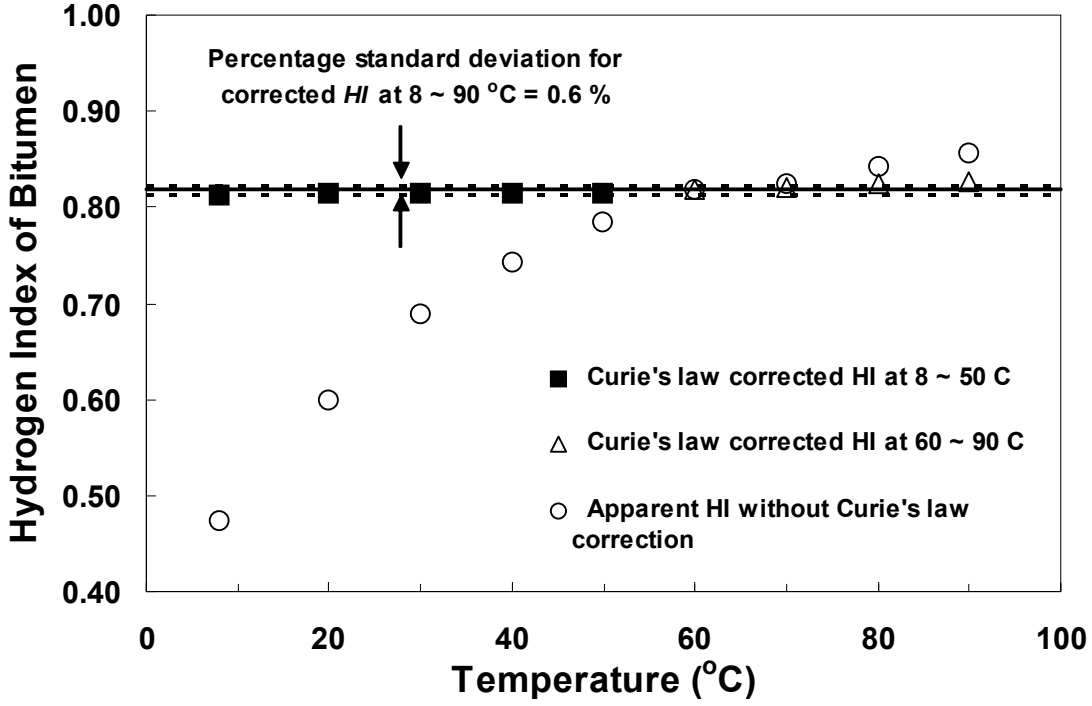

Fig. 17. Hydrogen Index of bitumen at different temperatures

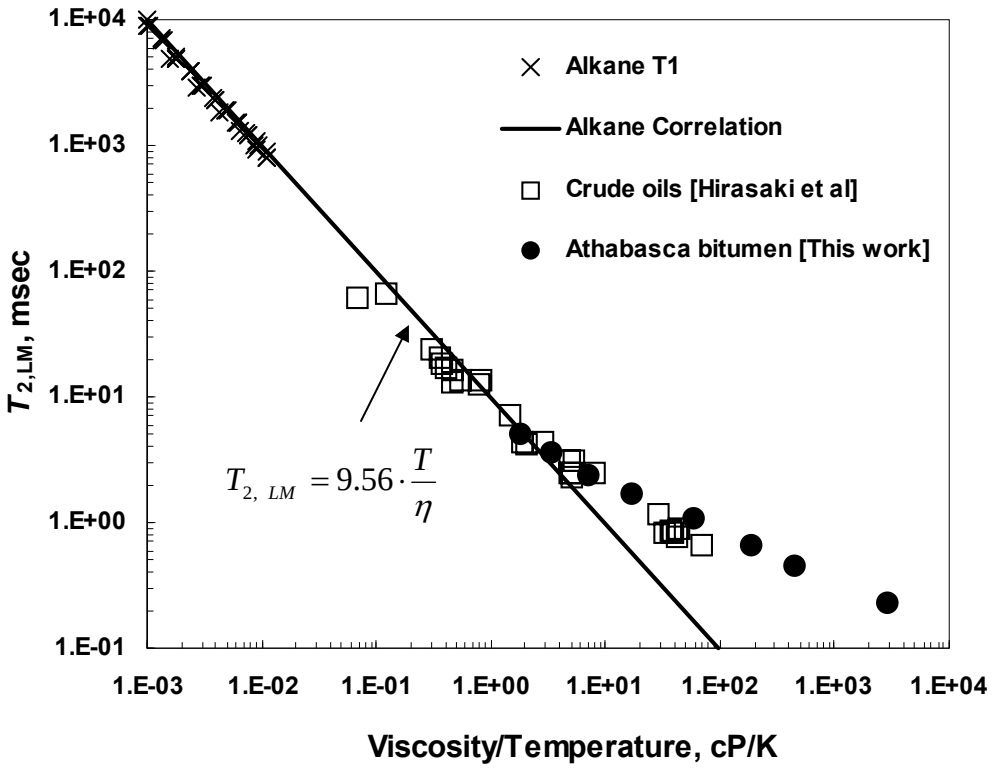

Fig. 18. Measured viscosity/temperature ratio of hydrocarbon vs. log-mean T_2.

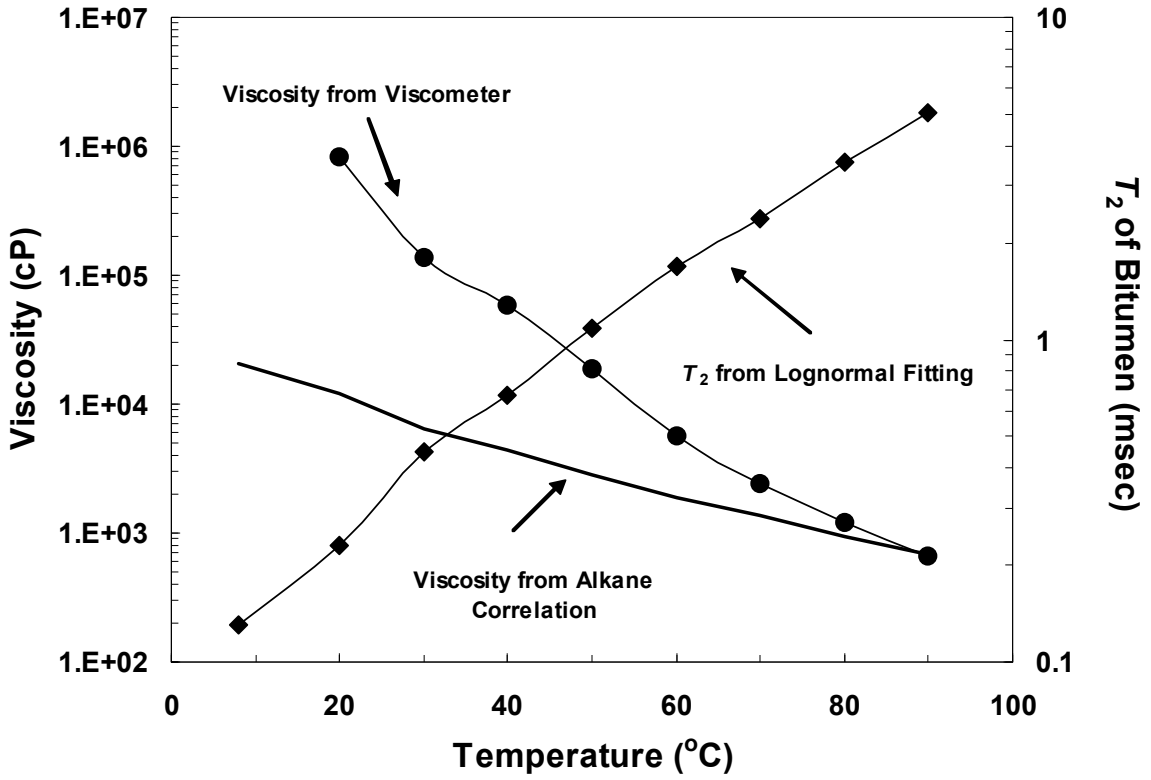

Fig. 19. Comparison on bitumen viscosity from two different methods

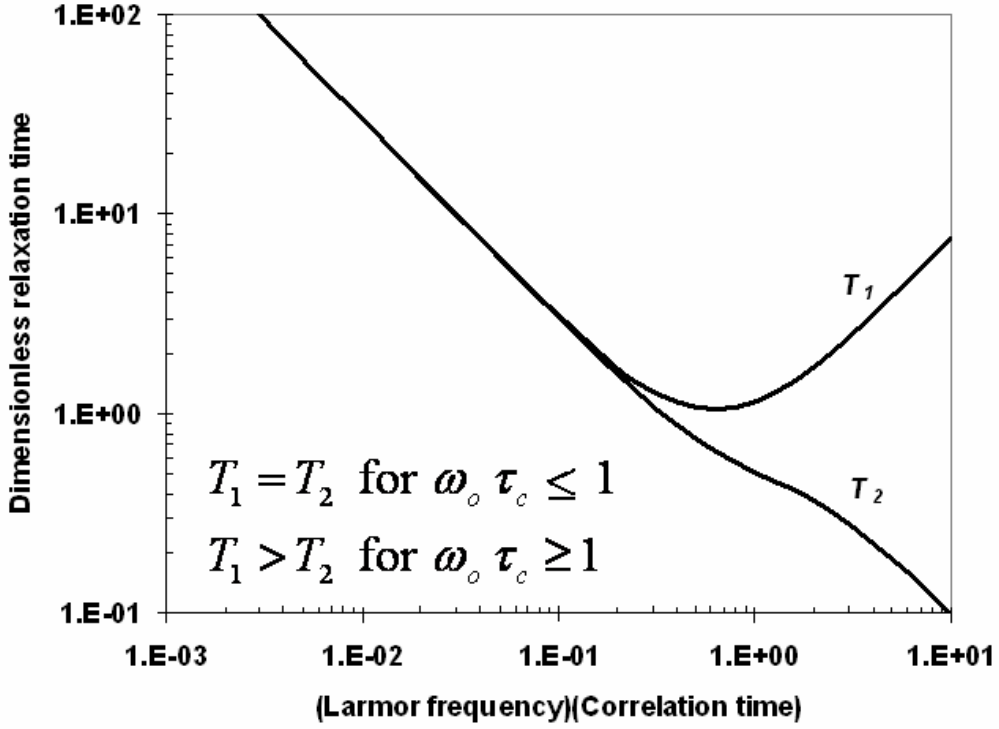

Fig. 20. Relationship between the dimensionless relaxation time and the product of Lamar frequency and correlation time (Hirasaki et al, 2003).

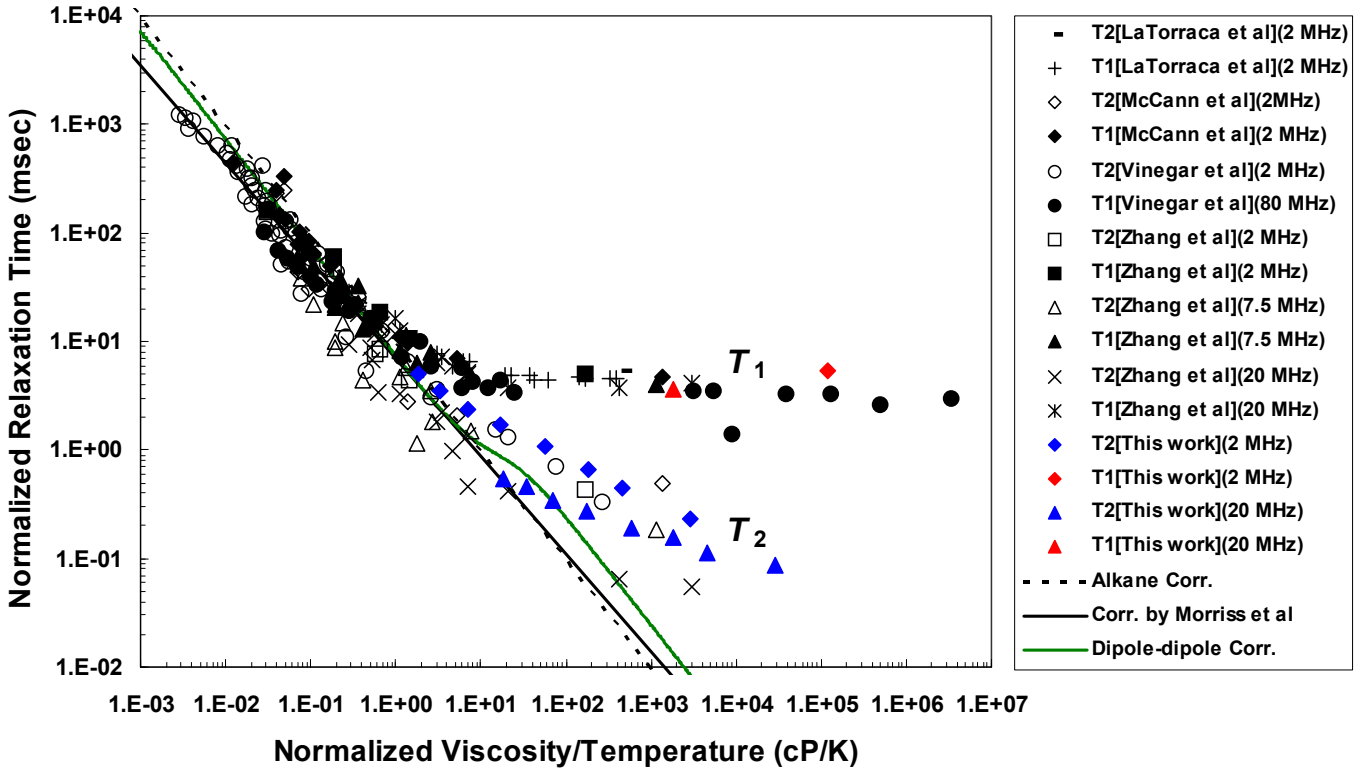

Fig. 21. Relationship between normalized relaxation times and normalized viscosity/temperature ratio.

Transverse relaxation in sandstones due to the presence of Internal Field Gradients

Neeraj Rohilla

Introduction

The presence of paramagnetic minerals in sandstone lead to enhanced Transverse relaxation because of Internal field gradients. In order to model the effect of Internal field gradients on Transverse relaxation due to the presence of clay flakes in sandstones, we consider a clay-lined pore as described in figure 1 and 2. Only one-fourth of the pore is considered because of the presence of symmetry boundary planes as marked in figure 1 and 2. The clay flake is assumed to be infinitely long in $\pm$ x directions. This strikes out any dependence of x co-ordinate and effectively makes the model two dimensional. η and λ are the aspect ratio for the macro-pore and clay flake respectively and β is the microporosity fraction.

The induced magnetic field due to the presence of clay flake is calculated using the procedure described by Zhang (2001). The following is the expression for the induced magnetic field.

$$B_{\delta z} = \frac{B_o \Delta\chi}{2\pi}\left[\begin{array}{l}\tan^{-1}\left(\frac{\lambda\left(\beta - z^*\right)}{y^*\beta - \lambda}\right) + \tan^{-1}\left(\frac{\lambda\left(\beta + z^*\right)}{y^*\beta - \lambda}\right) \\ -\tan^{-1}\left(\frac{\lambda\left(\beta - z^*\right)}{y^*\beta + \lambda}\right) + \tan^{-1}\left(\frac{\lambda\left(\beta + z^*\right)}{y^*\beta + \lambda}\right)\end{array}\right]$$

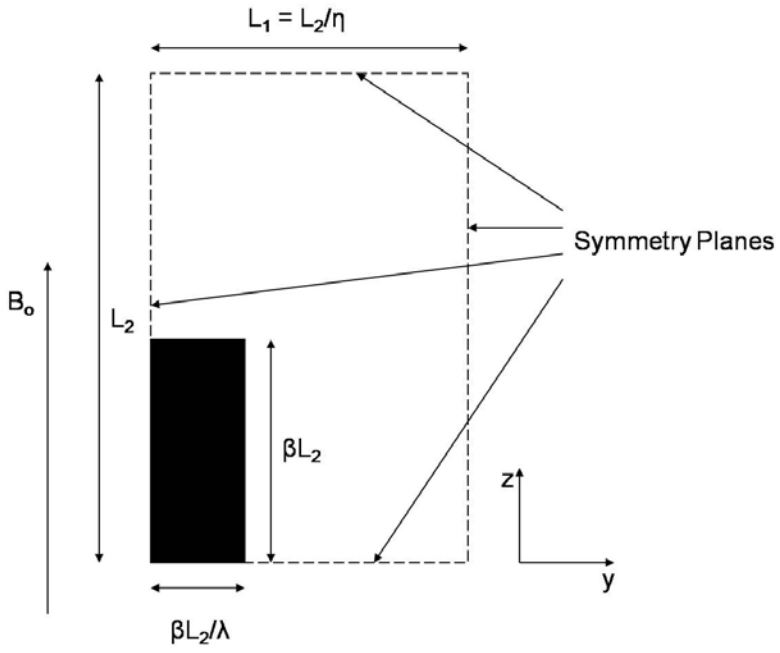

Figure1: Schematic of a clay-lined pore

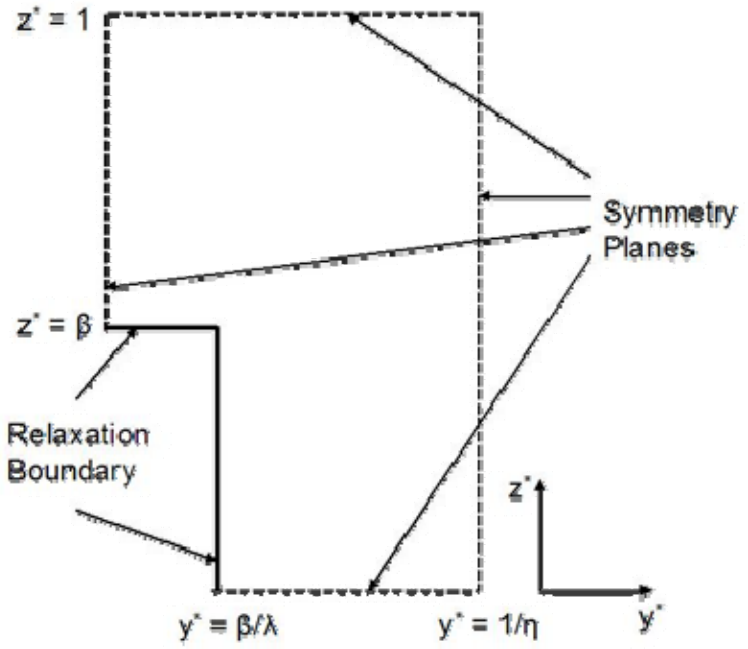

Figure 2: Schematic of the simulation domain

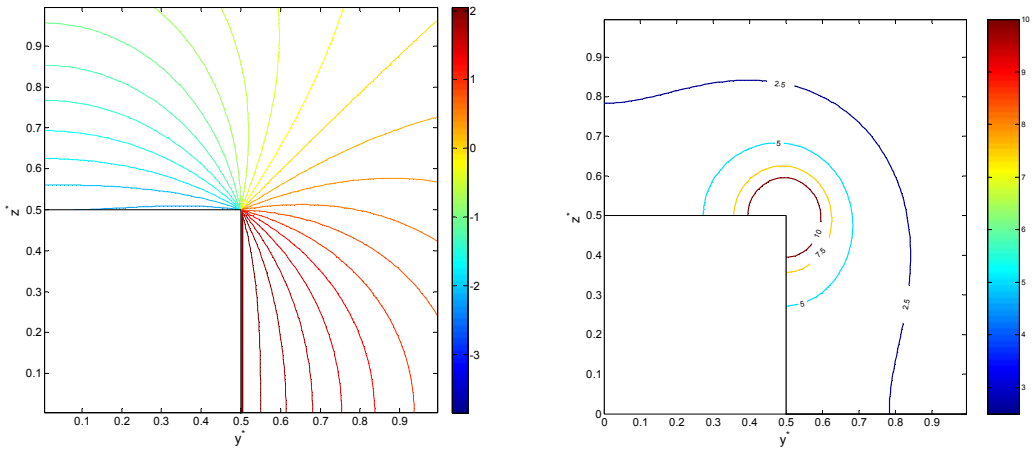

(a) (b)

Figure 3: (a) Contours of z component of induced magnetic field and (b) Contours of dimensionless gradient due to the presence of clay flake

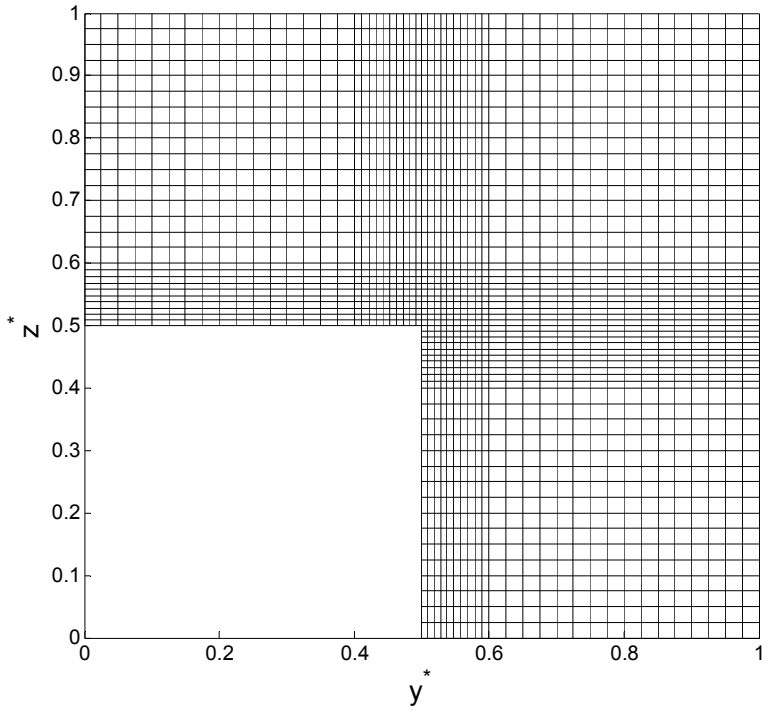

Figure 4: Schematic of mesh used to resolve large values of gradients around the corner

The gradient of induced magnetic field is made dimensionless using $\frac{B_o \Delta\chi}{2\pi L_2}$ as the characteristic value of the gradient. Figure 3 (a) shows the contours of the z component of the induced magnetic field due to the presence of a square shaped clay flake at the center of the pore. In order to better visualize the induced magnetic field, we also plot the contours of the dimensionless gradient of the induced magnetic field as shown in figure 3 (b). We observe very high gradients of induced field around the corner of the clay flake. In order to accurately capture high values of gradients, we use adaptive mesh in the simulation. Figure 4 shows the structure of the grid blocks used in the simulation. We use variable (logarithmic) grid spacing near the corner of the clay flake and uniform grid spacing for the rest of the domain. Using an adaptive mesh considerably reduces the simulation time.

Simulation for FID and CPMG pulse sequence:

This section describes the results for the simulation of the Free Induction Decay (FID) and Carr-Purcell-Meiboom-Gill (CPMG) pulse sequence for a macro-pore which contains a clay flake. The Transverse relaxation is simulated in y-z plane. We start with Bloch-Torrey equations for the transverse magnetization after the application of a 90^o pulse. The applied magnetic field is in the z direction, B_o.

Governing Equations:

$$\frac{\partial M_x}{\partial t} = \gamma M_y B_z - \frac{M_x}{T_{2B}} + D\nabla^2 M_x \tag{2}$$

$$\frac{\partial M_y}{\partial t} = -\gamma M_x B_z - \frac{M_y}{T_{2B}} + D\nabla^2 M_y \tag{3}$$

If we assume $M = M_x + iM_y$, then the above equations can be described by a single equation.

$$\frac{\partial M}{\partial t} = -\gamma M B_z - \frac{M}{T_{2B}} + D\nabla^2 M \tag{4}$$

When $M = m\exp\left[-i\omega_o t - \frac{t}{T_{2B}}\right]$ is substituted in equation 4, the equation is transformed into rotating co-ordinate frame and bulk relaxation term is factored out. The resulting equation is:

$$\frac{\partial m}{\partial t} = -\gamma m B_{\delta z} + D\nabla^2 m \tag{5}$$

Where, $B_{\delta z} = B - B_o$ and m is a complex variable, ($m = m_R + im_I$). $B_{\delta z}$ is given as:

$$B_{\delta z} = \frac{B_o \Delta\chi}{2\pi}\left[\begin{array}{l} \tan^{-1}\left(\frac{\lambda\left(\beta - z^*\right)}{y^*\beta - \lambda}\right) + \tan^{-1}\left(\frac{\lambda\left(\beta + z^*\right)}{y^*\beta - \lambda}\right) \\ -\tan^{-1}\left(\frac{\lambda\left(\beta - z^*\right)}{y^*\beta + \lambda}\right) + \tan^{-1}\left(\frac{\lambda\left(\beta + z^*\right)}{y^*\beta + \lambda}\right) \end{array}\right] \tag{6}$$

For the sake of convenience, now onwards we shall refer $B_{\delta z} = \frac{B_o \Delta\chi}{2\pi} F\left(y^*, z^*\right)$ so that the dependence of y^* and z^* is represented by $F\left(y^*, z^*\right)$. Thus we obtain:

$$\frac{\partial m}{\partial t} = -\frac{i\gamma B_o \Delta\chi}{2\pi} F\left(y^*, z^*\right) m + D\nabla^2 m \tag{7}$$

Boundary and Initial Conditions:

$\hat{n}.\nabla m = 0$: At symmetry planes

$D\hat{n}.\nabla m + \rho m = 0$: at micropore surface

$m(t=0) = m_o$: Uniform initial magnetization throughout the pore

Dimensionless groups and their significance:

The governing equations and boundary conditions are made dimensionless with characteristic scales, x^o, t^o and M^o. The characteristic scales and respective dimensionless variables are described below.

$x^o = L_2$: Half length of the macro-pore

$t^o = \tau_\omega = \dfrac{1}{\delta\omega} = \dfrac{1}{\lambda B_o \Delta\chi}$: Timescale for significant dephasing

$m^o = m_o$: Initial magnetization

$$m^* = \frac{m}{m^o}$$

$$y^* = \frac{y}{y^o}, z^* = \frac{z}{z^o}$$

$$t^* = \frac{t}{\tau_\omega}$$

$$\tau_E{}^* = \frac{\tau_E}{\tau_\omega} = \delta\omega\tau_E$$

$$\tau_R = \frac{L_2^2}{D}$$

Using dimensionless variables, the governing equations become:

$$\frac{\left(\frac{L_2^2}{D}\right)}{\left(\frac{1}{\gamma B_o \Delta\chi}\right)} \frac{\partial m^*}{\partial t^*} = \frac{-i}{2\pi} \frac{\left(\frac{L_2^2}{D}\right)}{\left(\frac{1}{\gamma B_o \Delta\chi}\right)} F\left(y^*, z^*\right) m^* + \nabla^{*2} m^* \tag{8}$$

$$\zeta \frac{\partial m^*}{\partial t^*} = \frac{-i}{2\pi} \zeta F(y^*, z^*) m^* + \nabla^{*2} m^* \tag{9}$$

Equation 9 contains the dimensionless group $\zeta = \dfrac{\left(\frac{L_2^2}{D}\right)}{\left(\frac{1}{\gamma B_o \Delta\chi}\right)}$ which is the ratio of two timescales present in the system. First is the diffusional correlation time $\tau_R = \dfrac{L_2^2}{D}$ and another is the time for significant dephasing, i.e. $\tau_\omega = \dfrac{1}{\gamma B_o \Delta\chi}$. Based on the relative magnitudes of these timescales, three different characteristic relaxation regimes are defined as follows:

1) Motionally averaging regime: In this regime, Diffusional correlation time, τ_R is the smallest timescale. Field inhomogeneities are motionally averaged and hence Transverse relaxation rate does not show any dependence on echo spacing.
2) Localization regime: In this regime, time for significant dephasing, τ_ω is the smallest timescale and Transverse relaxation rate is strongly dependent on echo spacing.
3) Free diffusion regime: This regime is characterized by half echo-spacing, τ_E being the smallest timescale and Transverse relaxation rate follows quadratic dependence on echo spacing.

Equation 9 with given Boundary and initial conditions is solved using Alternating Direction Implicit (ADI) method. For CPMG pulse sequence simulation, the third characteristic timescale is the dimensionless echo spacing, $\tau_E^* = \frac{\tau_E}{\tau_\omega}$. The dependence of timestep was checked and optimum value of the timestep was used for all simulations. The subsequent sections discuss the results for FID and CPMG pulse sequence.

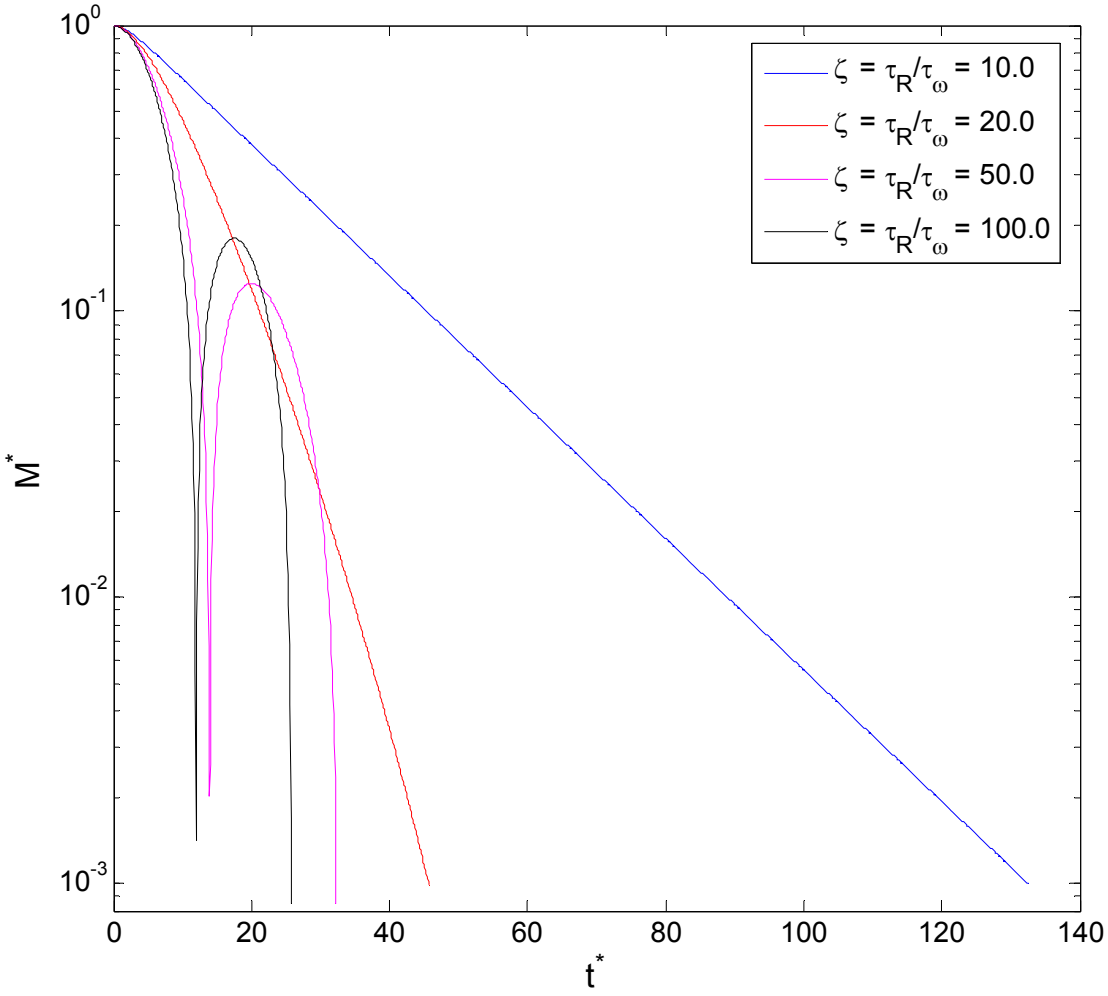

Figure 5: Decay of the magnitude of magnetic moment versus dimensionless time for different values of $\zeta = \frac{\tau_R}{\tau_\omega}$

Figure 5 show the decay of magnitude of magnetic moment for different values of $\zeta = \frac{\tau_R}{\tau_\omega}$. When the values of ζ is more than 20, the FID is not monotonically decreasing. The magnitude of magnetic moment drops by two orders of magnitude and begins to rise again. These undulations finally die out in the noise level. It is interesting to see that the amplitude of these undulations is not small. For first undulation, it reaches the magnitude of ~0.2 before starting to go down again.

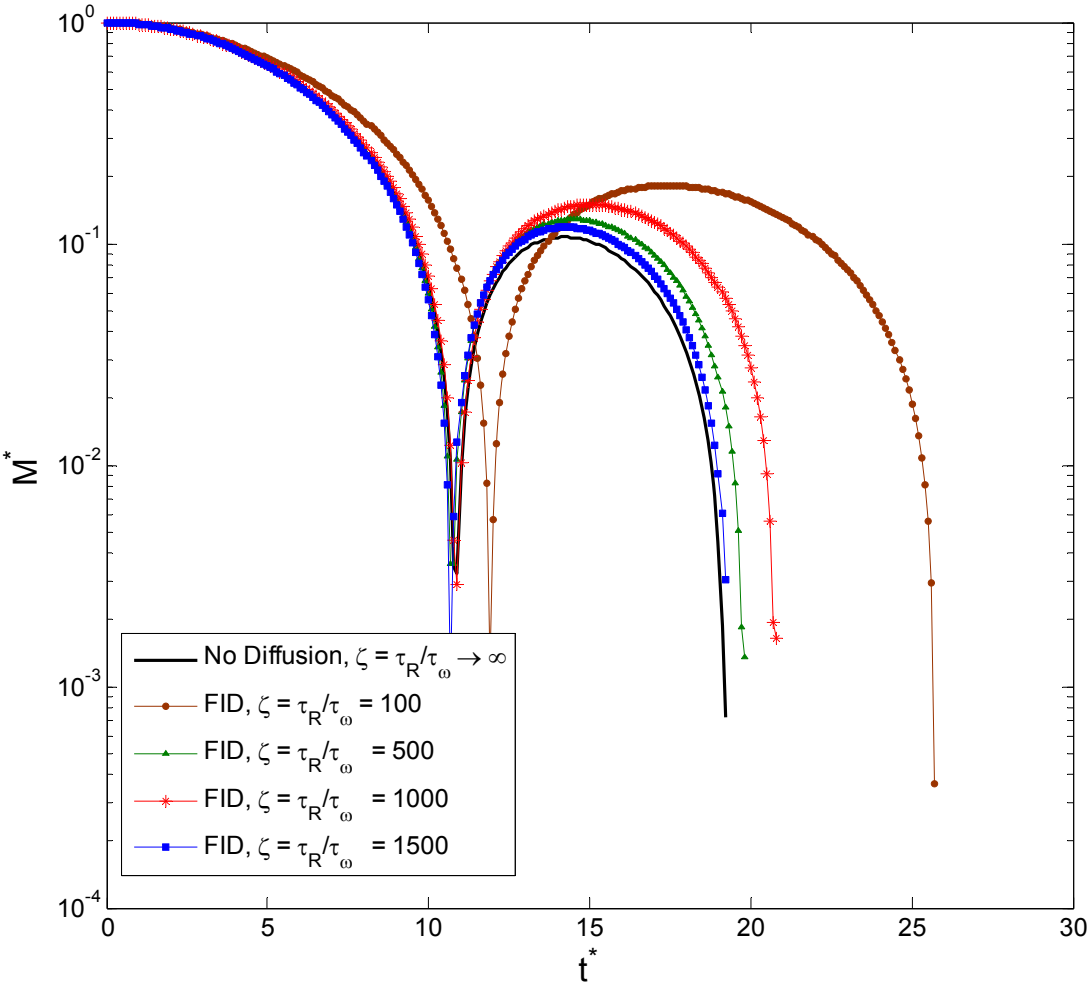

Figure 6: Comparison of FID decay of magnitude of magnetization for different values of ζ and for the case when no diffusion is present

The small value of ζ corresponds to large value of diffusion coefficient and fast diffusion of molecules. Because of this fast diffusion molecules sample different Larmor frequencies at different locations and this leads to a single exponential decay. However, large value of ζ means slow diffusion and proton do not sample a range of Larmor frequencies. Hence protons of different molecules have different Larmor frequencies and when they are out of phase from one another, we see the decay of magnetization. However, when the protons are in phase with one another, the magnitude of magnetization starts to build up again and finally decays due to relaxation.

In order to fully test this hypothesis, we can switch off diffusion for current case. This simplifies the equations significantly and we have a first order differential equation which can be solved using implicit Euler method. We should recover this solution in the limit of large value of ζ, because large value of ζ means slow

diffusion. Figure 6 shows decay of magnitude of magnetic moment for the case when diffusion is switched off and for different values of ζ. We observe that the simulation for higher values of ζ match very well with the case for no diffusion. This confirms our hypothesis and suggests that in the presence of internal field gradients, we can actually observe FID data which does not decay monotonically.

CPMG results and discussion:

The existing program for FID can be easily modified for CPMG pulse sequence. For CPMG pulse sequence, at $t = \tau_E$ we apply a 180^o pulse which is equivalent to $m\left(t = \tau_E^+\right) = \bar{m}\left(t = \tau_E^-\right)$ where $\bar{m}$ represents the transpose of the m. Figure 7 shows the decay of magnitude of magnetization for CPMG pulse sequence with $\zeta = \frac{\tau_R}{\tau_\omega} = 100$ and dimensionless echo spacing, $\tau_E^* = 5.0$. Figure 7 demonstrates that 180^o pulses refocus the magnetization and results in smaller relaxation rates than those for Free Induction Decay.

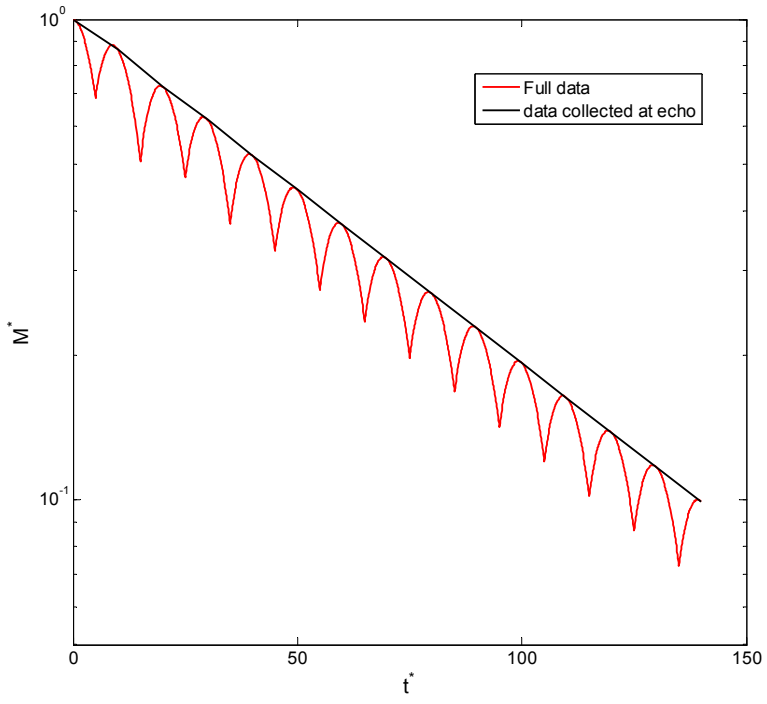

Figure 7: Plot for CPMG decay of magnitude of magnetization for dimensionless echo spacing, $\tau_E^* = 5.0$ and $\zeta = \frac{\tau_R}{\tau_\omega} = 100$

We summarize our results in terms of two parameters. First is ζ which is the ratio of τ_R and τ_ω and second is dimensionless half-echo spacing, τ_E^* which is the ratio of τ_E and τ_ω. We fit a single-exponential curve for the decay of magnetic moment and calculate dimensionless Transverse relaxation rate for each parameter value. The magnetization decay is bi-exponential for the simulations where $\zeta = \frac{\tau_R}{\tau_\omega}$ is more than 1000. A few of these cases are illustrated in figures 8, 9 and 10.

For such cases, slower component of bi-exponential decay is taken as the relaxation rate. Using these values of the dimensionless Transverse relaxation rate, we create a single plot which shows the relaxation rates for all parameter values which is illustrated in figure 11. In figure 11, for motionally averaging regime where τ_R is the smallest timescale, relaxation rates are independent of echo spacing. For Localization regime where τ_ω is the smallest timescale, relaxation rates are strongly dependent on echo spacing.

We observe that for τ_E^* less than one and values of ζ higher than 100, we see that relaxation rates are not dependent on ζ or τ_E^*. This observation is in contrast with the results reported by Anand (2007) in figure 12. We are still investigating the reasons for this behavior and this issue will be explained in detail in the next weekly report.

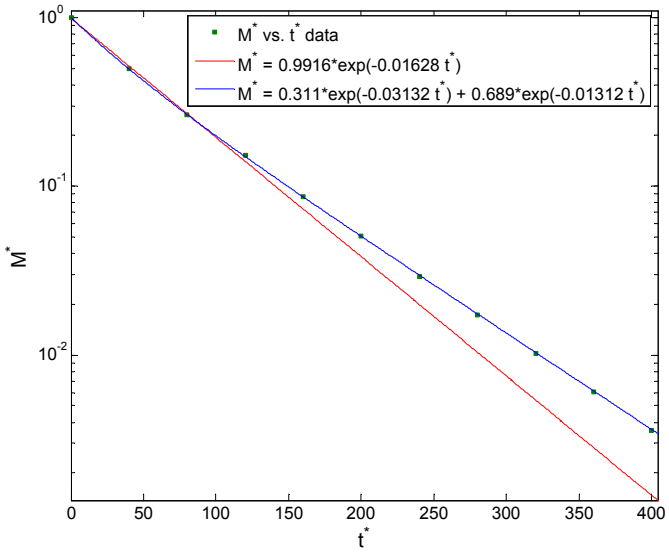

Figure 8: Bi-exponential plot for $\zeta = 1390, \tau_E^* = 20.0$

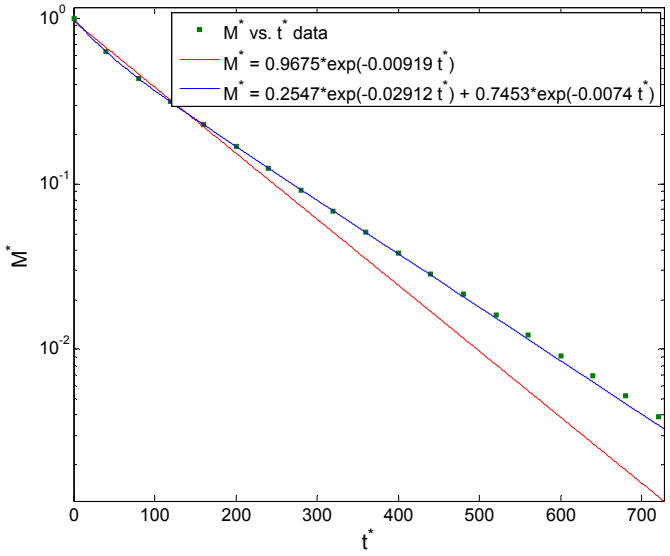

Figure 9: Bi-exponential plot for $\zeta = 2683, \tau_E^* = 20.0$

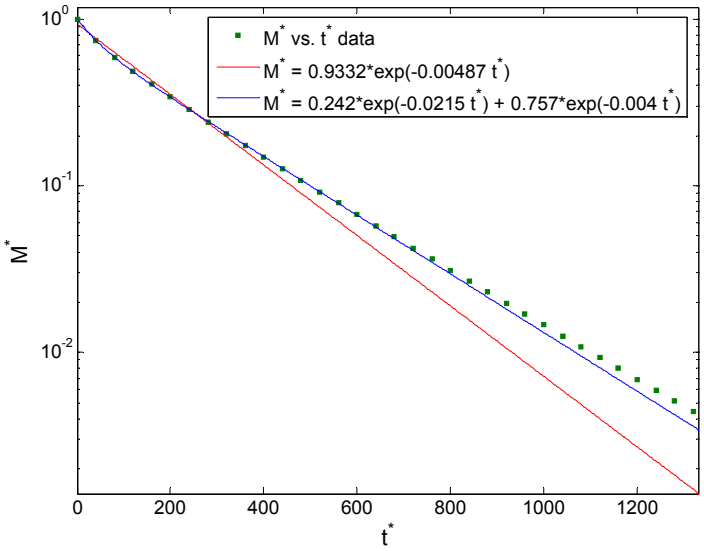

Figure 10: Bi-exponential plot for $\zeta = 5180, \tau_E^* = 20.0$

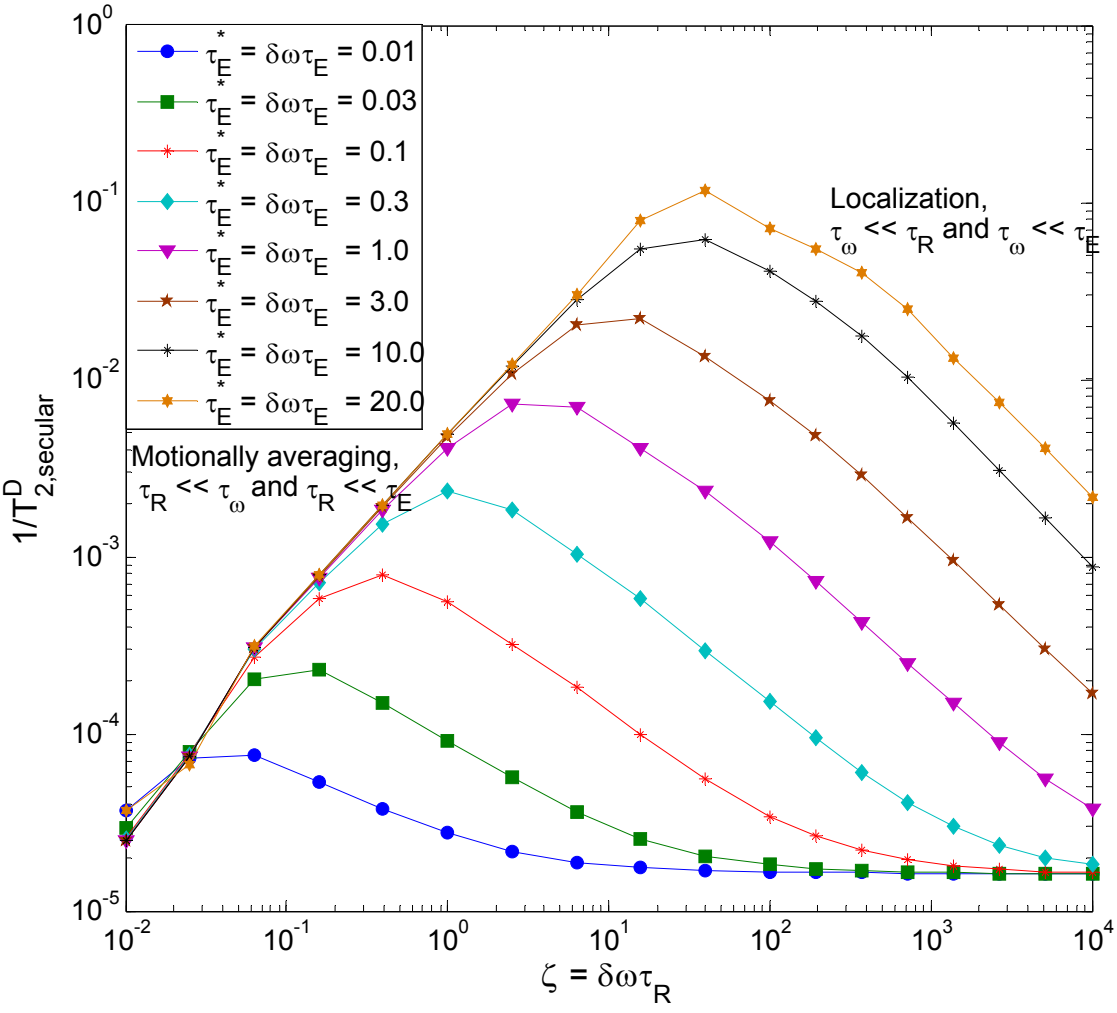

Figure 11: Plot of simulated relaxation rate (dimensionless) with $\zeta = \frac{\tau_R}{\tau_\omega}$ as a function of $\tau_E^* = \frac{\tau_E}{\tau_\omega}$

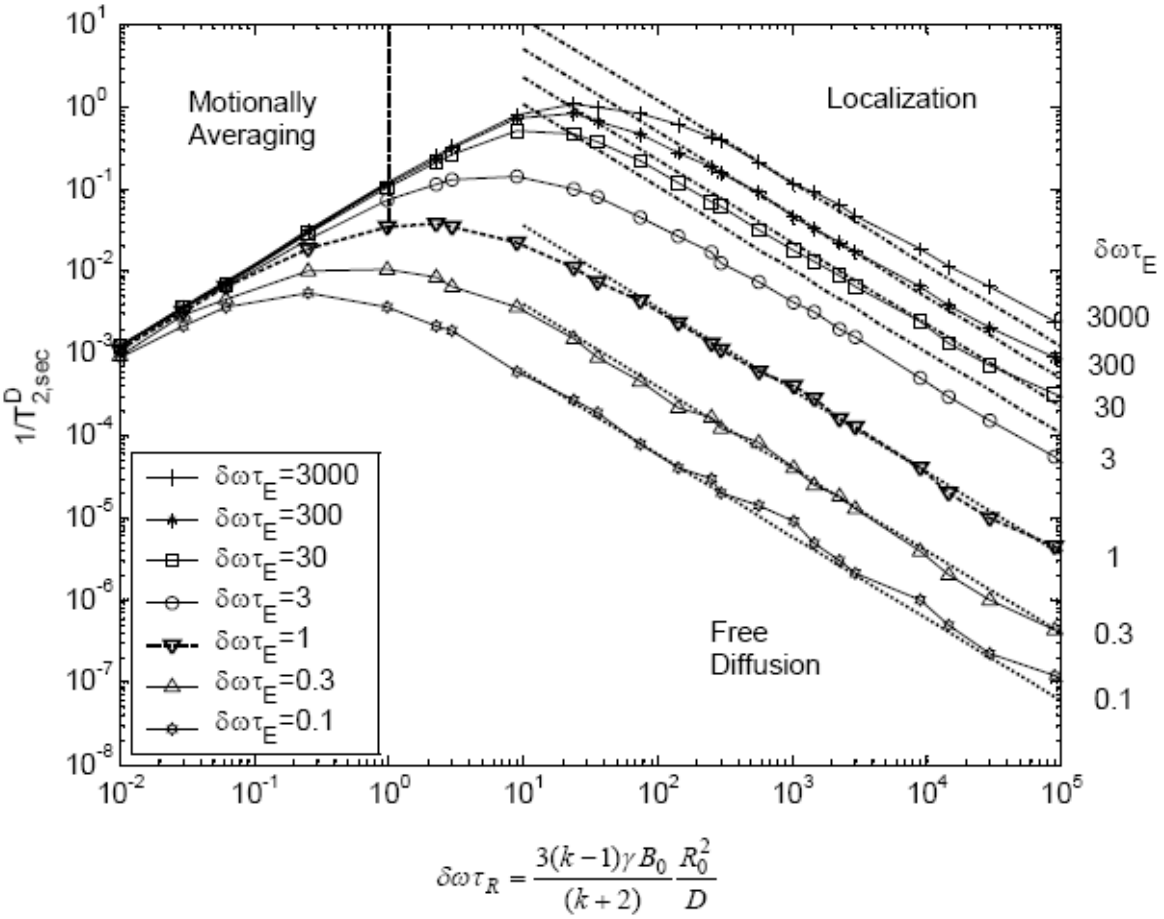

Figure 13: Plot of simulated relaxation rate (dimensionless) with $\delta\omega\tau_R$ as a function of $\delta\omega\tau_E$ (Anand (2007))

References

Anand, V. 2007 NMR Oil Well Logging: Diffuusion Coupling and Internal Gradients in Porous Media. *PhD Thesis*.

Zhang, Q. 2001 NMR Formation Evaluation: Hydrogen Index, Wettability and Internal Field Gradients. *PhD Thesis*.

Summary of Accomplishments; Years 1 and 2

The accomplishments of this project are summarized by brief statements following the deliverables of the project.

Task 1. Properties of reservoir fluids

Subtask 1.1 Properties of live reservoir fluids

NMR High Pressure Measurements for Natural Gas Mixtures
A manifold has been built for making NMR measurements at high pressures up to 5000 psi. Separate relaxation time and diffusivity measurements are shown for methane gas at elevated pressure for comparison with values from other investigators. Methane relaxation times approaching the expected trend from the literature have been obtained. However the relaxation times obtained are consistently smaller than reported values. The measured diffusivity is consistent within the measurements in this work; however the value is 20% less than the correlated value from Prammer, *et al.* (1995). The diffusivity data do not appear to match the correlation within the scatter of the data. The reason for this is unknown.

Subtask 1.2 Properties of oil-based drilling fluids (Kurup and Hirasaki, 2005)

Oil-based drilling fluids can invade formations and contaminate crude oils, hindering logging analysis. This work details ^{1}H NMR T_2 measurements with mixtures of one drilling-fluid base oil, NovaPlus (SNP), and crude oils to determine the effect of the contamination. Measurements are made using 2 MHz MARAN bench-top instruments on mixtures having various concentrations of SNP, with each of three crude oils (labeled STNS, SMY, and PBB), whose viscosities range from 13.7 to 207 cp. T_2 measurements for mixtures containing SMY and SNP are repeated four times for purpose of statistical analysis.

Two approaches are explored to better relate NMR measurements with contamination. In the first approach, a selective contamination index (SCI) is defined that relates the T_2 distribution to the contamination. Here, a subset of the T_2 data is chosen for analysis based on sensitivity to contamination. In the second approach, the T_2 data are fit to a four-parameter, skewed Gaussian model for T_2 distributions. Two parameters of the model are combined in a distribution parameter index (DPI), which can be related to contamination.

Both the SCI and DPI values can be fit using cubic polynomials, resulting in a functional dependence on concentration. The polynomial functions, used in reverse, yield estimations of the degree of contamination, which for SMY-SNP mixtures are compared to standard

$T_{2,LM}$ methods. The comparison of the $T_{2,LM}$, SCI, and DPI methods is done in terms of the estimated error in the degree of contamination. The SCI method provides the best estimate of contamination.

Task 2. Estimation of fluid and rock properties and their interactions from NMR relaxation and diffusion measurements

Subtask 2.1 Extend the diffusion editing technique and interpretation (Flaum, 2003)

Restricted diffusion measurements have the potential to measure size and connectivity between pores. A method was developed to estimate the relaxation time and size distribution of a system of spheres. A single set of NMR diffusion parameters is sensitive to only a limited range of sphere sizes. Thus a multiple sets of NMR parameters are required to estimate a wide distribution of sphere sizes. The results from each set are combined use of a mask that limits inclusion of only valid results. This results in a composite map of T_2 and sphere size.

Subtask 2.2 Application of restricted diffusion for characterization of vuggy carbonate formations (Flaum, 2003)

Interpretations of carbonate rock and sandpacks were ambiguous because of the difficulty of obtaining fluids and parameters over a wide enough range. However, the method was successful in estimating the drop size distribution of water in oil emulsion (Aichele, *et al*., 2007).

Subtask 2.3 Interpretation of systems with significant internal magnetic field gradients

Paramagnetic relaxation in sandstones: Distinguishing T_1 and T_2 dependence on surface relaxation, internal gradients and dependence on echo spacing (Anand and Hirasaki, 2007)

This work provides a generalized theory of proton relaxation in inhomogeneous magnetic fields. Three asymptotic regimes of relaxation are identified depending on the shortest characteristic time scale. Numerical simulations illustrate that the relaxation characteristics in the regimes such as the T_1/T_2 ratio and echo spacing dependence are determined by the time scales. The theoretical interpretation is validated for fluid relaxation in porous media in which field inhomogeneity is induced due to susceptibility contrast of fluids and paramagnetic sites on pore surfaces. From a set of measurements on model porous media, we conclude that when the sites are small enough, no dependence on echo spacing is observed with conventional low-field NMR spectrometers.

Echo spacing dependence is observed when the paramagnetic materials become large enough or form a 'shell' around each grain such that the length scale of the region of induced magnetic gradients is large compared to the diffusion length during the time of the echo spacing. The theory can aid in interpretation of diffusion measurements in porous media as well as imaging experiments in presence of contrast agents used in MRI.

Subtask 2.4 Interpretation of systems with diffusional coupling between pores

Diffusional Coupling Between Micro and Macroporosity for NMR Relaxation In Sandstones and Grainstones (Anand and Hirasaki, 2007)

Pore structure analysis by NMR relaxation assumes that the T_1 or T_2 distribution is directly related to the pore size distribution. This assumption breaks down if the fluid in different sized pores is coupled through diffusion. In such cases, the estimation of formation properties such as permeability and irreducible water saturation using the traditional $T_{2,cutoff}$ method would give erroneous results. Several techniques like "spectral" BVI and tapered $T_{2,cutoff}$ have been introduced to take into account the effects of diffusional coupling for better estimation of properties.

In this paper, we aim to provide a theoretical and experimental understanding of NMR relaxation in systems with diffusionally coupled micro- and macropores. Relaxation is modeled such that the fluid molecules relax at the surface of micropores and simultaneously diffuse between the two pore types. The T_2 distribution of the pore is a function of several parameters including micropore surface relaxivity, fluid diffusivity and pore geometry. The governing parameters are combined in a single coupling parameter (α) which is defined as the ratio of the characteristic relaxation rate of the pore system to the rate of diffusional mixing of fluid molecules between micro- and macropores. It is shown that depending on the value of α, the two pore types can communicate through total, intermediate or decoupled regimes of coupling.

The model is applied to treat diffusional coupling in sandstones with a distribution of macropores lined with clay flakes. Simulations are verified by comparing with experimental results for chlorite coated, North-Burbank sandstone. It is observed that the T_1 distribution shows a bimodal distribution at 100% water saturation but a unimodal distribution when saturated with hexane. This occurs because the extent of coupling is higher for hexane than for water due to lower relaxivity and higher diffusivity of hexane. The α values indicate intermediate coupling for water and strong coupling for hexane.

The model is also applied to grainstone carbonates with intra and intergranular porosity. In this case, α is found to have a quadratic

dependence on grain radius and inverse dependence on micropore radius. The theory is experimentally validated on several systems with microporous particles of varying grain diameters and known microporosities. Here too, the T_2 distribution at 100% water saturation varies from bimodal for coarse-grained particles to unimodal for fine-grained particles. The transition from bimodal to unimodal distribution is also predicted theoretically from the values of α.

Subtask 2.5 Quantify the mechanisms responsible for the deviation of surface relaxivity from the mean value for sandstones and carbonates

(See Subtasks 2.3 and 2.4)

Subtask 2.6 Quantify native formation wettability and the effects of wettability alteration due to invasion of oil-based drilling fluid filtrate

NMR wettability indices: Effect of OBM on wettability and NMR responses (Chen, et al., 2006)

Wettability and NMR surface relaxation are related to each other. Wettability controls the fluid distribution in porous media. NMR surface relaxation dictates that the fluid in contact with the mineral surface has a relaxation time shorter than its bulk value. In this study, first, the nature of wettability effect on NMR responses was demonstrated by a parameter $\rho_{2,eff}$, the effective surface relaxivity. Quantitative changes of $\rho_{2,eff}$ of water or oil for unconsolidated silica flour and calcite were shown to be consistent with the expected wettability alteration based on the contact angle measurements. Based on the concept of effective surface relaxivity, a novel NMR model was then proposed to quantify rock wettability by two NMR wettability indices from either water or oil responses. This model was tested with water/oil partially saturated Berea cores at different wettability conditions. Correlations show that both NMR indices agree well with the Amott–Harvey wettability index, suggesting that quantitative information of reservoir rock wettability can be gained from NMR measurements. Finally, the effect of oil base mud (OBM) surfactants on wettability alteration and NMR responses was systematically investigated with Berea cores. Results show that the originally strongly water-wet Berea cores are altered to be intermediate-wet or oil-wet by OBM surfactants. As a result, the irreducible water saturation from NMR interpretation assuming water-wetness when wettability alteration occurs generally underestimates the measured value. The magnitude of underestimation correlates well with the Amott–Harvey wettability index.

Task 3. Characterization of Pore Structure and Wettability

Subtask 3.1 Pore Structure (Hidajat, et al., 2004)

Characterization of pore structure and wettability has been completed on six carbonate samples. The vug size, distribution and interconnection vary significantly in these six samples. The thin sections

have been characterized through their pore size distribution, two-point correlation function, chord number distribution, lineal path function and fractal dimension. The power spectrum from Fourier transform has been computed. The three-dimensional pore structures have been reconstructed for two carbonates and one sandstone sample. Single phase permeability and NMR response has been measured for all the samples. The relative permeability, NMR response and electrical conductivity have been measured for three samples.

Subtask 3.2 Wettability (no progress)

Subtask 3.3 NMR Response Modeling (no progress)

Subtask 3.4 Enhanced Spontaneous Imbibition (no progress)

Task 4. Characterization of Multiphase Transport Properties (no progress)

Subtask 4.1 Relative Permeability and Electrical Conductivity

Subtask 4.2 Pore-Network Modeling

Subtask 4.3 Permeability / Relative Permeability Correlation

Subtask 4.4 Characterization of flowing fraction in multiphase flow

Task 5. Technology Transfer (see publications)

REFERENCES

Aichele, C. P., Flaum, M., Jiang, T., Hirasaki, G. J., Chapman, W. G., "Water in oil emulsion droplet size characterization using a pulsed field gradient with diffusion editing (PFG-DE) NMR technique," *JCIS* **315** (2007) 607-619.

Anand, V. and Hirasaki, G.J., "Diffusional Coupling between Micro and Macroporosity for NMR Relaxation in Sandstones and Grainstones," *Petrophysics,* **48**.4 (2007) 289-307.

Anand, V. and Hirasaki, G. J., "Paramagnetic relaxation in sandstones: Distinguishing $T_1$and T_2 dependence on surface relaxation, internal gradients and dependence on echo spacing," *Journal of Magnetic Resonance*, *Available online 4 October 2007.*

Chen, J., Hirasaki, G.J., Flaum, M., "NMR wettability indices: Effect of OBM on wettability and NMR responses," *J. Pet. Sci. & Eng*., 52 (2006) 161-171.

Flaum, M., Fluid and Rock Characterization Using New NMR Diffusion-Editing Pulse Sequences and Two Dimensional Diffusivity-T_2 Maps, PhD thesis, Rice University, 2003

Flaum, M., Chen, J., and Hirasaki, G. J., "NMR Diffusion Editing for D-T_2 Maps: Application to Recognition of Wettability Change," *Petrophysics*, Vol. **46**, No. 2 (April 2005), 113-123.

Hidajat, I., Mohanty, K.K., Flaum, M., and Hirasaki, G. J., "Study of Vuggy Carbonates Using NMR and X-Ray CT Scanning," *SPE RE&E*, (October 2004), 365-377.

Hirasaki, G. J., "NMR Applications in Petroleum Reservoir Studies," in *NMR Imaging in Chemical Engineering*, S. Stapf and S.-I. Han, Wiley-VCH (2006), 321-340.

Kurup, A. and Hirasaki, G. J., "Effect Of Drilling-Mud Base-Oil Contamination On Crude Oil T_2 Distributions," SPWLA 46th Annual Logging Symposium, June 26-29, 2005

Yang, Z. and Hirasaki, G. J., "NMR Measurement of Bitumen at Different Temperatures," accepted for publication in Journal of Magnetic Resonance, JMR-08-10R1 (March 17, 2008)